Olfactory flow in the sturgeon is externally driven

DOI:
10.1016/j.cbpa.2019.06.013

Document Version
Accepted author manuscript

Published in:
Comparative Biochemistry and Physiology. Part A: Molecular & Integrative Physiology

Olfactory Flow in the Sturgeon is Externally Driven

Russell J. Garwood[a], Julia Behnsen[b], Harriet K. Haysom[c], Jeremy N. Hunt[d], Luke J. Dalby[e], Samuel K. Quilter[e], James S. Maclaine[f], Jonathan P. L. Cox[c*]

[a]*School of Earth and Environmental Sciences, University of Manchester, Manchester, M13 9PL, UK*

[b]*Henry Moseley X-ray Imaging Facility, University of Manchester, Manchester, M13 9PY, UK*

[c]*Department of Chemistry, University of Bath, Bath, BA2 7AY, UK*

[d]*Jeremy Hunt Design, Unit A6, 66 Norlington Road, London, E10 6LA, UK*

[e]*TotalSim, Top Station Road, Brackley, NN13 7UG, UK*

[f]*Department of Life Sciences, Natural History Museum, Cromwell Road, London, SW7 5BD, UK*

Running title: Olfactory flow in the sturgeon

MS has 48 pages, 16 figures, 1 video, 1 appendix

Declaration of interest: None

*Corresponding author
Dr Jonathan P.L. Cox
Department of Chemistry
University of Bath
Bath, BA2 7AY, UK
Tel. +44 1225 386548
j.p.l.cox@bath.ac.uk

Abstract

Fluid dynamics plays an important part in olfaction. Using the complementary techniques of dye visualisation and computational fluid dynamics (CFD), we investigated the hydrodynamics of the nasal region of the sturgeon *Huso dauricus*. *H. dauricus* offers several experimental advantages, including a well-developed, well-supported, radial array (rosette) of visible-by-eye olfactory sensory channels. We represented these features in an anatomically accurate rigid model derived from an X-ray scan of the head of a preserved museum specimen. We validated the results from the CFD simulation by comparing them with data from the dye visualisation experiments. We found that flow through both the nasal chamber and, crucially, the sensory channels could be induced by an external flow (caused by swimming *in vivo*) at a physiologically relevant Reynolds number. Flow through the nasal chamber arises from the anatomical arrangement of the incurrent and excurrent nostrils, and is assisted by the broad, cartilage-supported, inner wall of the incurrent nostril. Flow through the sensory channels arises when relatively high speed flow passing through the incurrent nostril encounters the circular central support of the olfactory rosette, decelerates, and is dispersed amongst the sensory channels. Vortices within the olfactory flow may assist odorant transport to the sensory surfaces. We conclude that swimming alone is sufficient to drive olfactory flow in *H. dauricus*, and consider the implications of our results for the three other extant genera of sturgeons (*Acipenser*, *Pseudoscaphirhynchus* and *Scaphirhynchus*), and for other fishes with olfactory rosettes.

Keywords: 3D printing; *Aphanopus carbo*; Chimaeridae; Hexanchidae; micro-computed tomography; pressure coefficient; static pressure; streamline.

1. Introduction

As part of our ongoing programme to understand the fluid dynamic processes that govern the transport of odorant molecules to a fish's olfactory sensory surface (Cox, 2008; Abel et al., 2010; Holmes et al., 2011; Cox, 2013; Rygg et al., 2013; Howard et al., 2013; Agbesi et al., 2016a, 2016b), we report here the hydrodynamics of the sturgeon's nasal region. There has been no previous experimental work in this area. There has, however, been work in other areas of sturgeon olfaction (Kasumyan, 2004), e.g. on the nasal morphology (Chen and Arratia, 1994), and the olfactory epithelium (Pyatkina, 1975; Devitsyna and Kazhlayev, 1992; Zeiske et al., 2003; Hansen and Zielinski, 2005; Camacho et al., 2010).

We chose to investigate the hydrodynamics of the sturgeon's nasal region for several reasons. First, the nasal anatomy of the sturgeon (Fig. 1) suggests that flow of water through the nasal chamber may be driven by an external flow (Cox, 2008), and external flows (arising from, for example, the movement of the sturgeon as it swims forward) are relatively straightforward to replicate experimentally (Abel et al., 2010; Agbesi et al., 2016a, 2016b). Second, although we have shown that flow through the nasal chamber of a fish can be driven by an external flow (Abel et al., 2010), we have not previously investigated, in a physical model at least, the hydrodynamics in a fish's olfactory sensory channels (Fig. 1D and F, SC; a sensory channel is the region between two adjacent olfactory lamellae, highlighted by dashed lines in Fig. 1F; the olfactory epithelium is located on the surface of the olfactory lamellae). The sturgeon's well-developed radial array of olfactory lamellae ('olfactory rosette') – with distinct sensory channels that are visible through both the incurrent nostril and, in particular, the excurrent nostril (Fig. 1C-F) – afforded us an opportunity to do so. Third, because the sturgeon's olfactory lamellae appear well supported (Fig. 1C and D), they are unlikely to be deflected significantly by water flowing over or between them, and could therefore be faithfully represented by a rigid model. Finally, the olfactory hydrodynamics of the sturgeon are relevant to other fishes with olfactory rosettes, e.g. *Aphanopus carbo* (Holl and Meinel, 1968).

Our aim was to answer the following questions. 1) Can an external flow induce flow through the nasal chamber? 2) If so, what is the physical mechanism driving this flow? 3) Can an external flow induce flow through the sensory channels? 4) If so, what is the physical mechanism driving this flow?

We addressed both questions by a) using dye to visualise olfactory flow in a plastic model of the sturgeon's head, and by b) simulating flow in a computational model of the sturgeon's head (computational fluid dynamics, CFD; Tu et al., 2018). For dye visualisation, the forward motion of the fish was simulated by flowing water over the static model in a flume (Agbesi et al., 2016b). We used both dye visualisation and CFD because the two techniques are complementary. Dye visualisation gives an overall impression of flow behaviour (Lim, 2000; Settles, 2005), especially around an object with a complex geometry, such as the nasal region of a fish (Abel et al., 2010; Agbesi et al., 2016a, 2016b). CFD can give the static pressure on the surface of an object, but also within a fluid, allowing one to calculate, for example, the difference in pressure between an incurrent and an excurrent nostril (Rygg et al., 2013). CFD also gives the velocity of flow, allowing one to calculate Reynolds numbers, and to visualise flow using streamlines. Streamlines may in turn help to interpret the dye visualisation experiments, to visualise flow in regions that are obscured from the observer in a physical model, and to reveal flow behaviour not apparent from the dye visualisation experiments. Finally, CFD may overcome some of the limitations of dye visualisation. But, the CFD results must be validated by a comparison with the dye visualisation results, e.g. by replicating dye behaviour with CFD-generated streamlines.

There are four extant genera of sturgeons (family Acipenseridae): *Acipenser*, *Pseudoscaphirhynchus*, *Scaphirhynchus*, and *Huso* (Nelson, 2006). The plastic model and the computational model that we used in our study were both derived from an X-ray scan of a preserved specimen of *Huso dauricus*, a highly active swimmer (Vecsei and Peterson, 2004) found in a variety of aquatic habitats (estuarine, riverine, coastal; Krykhtin and Svirskii, 1997). We derived the models from this particular specimen because it had the best preserved olfactory rosette of all the sturgeon specimens that we inspected. We relate our results from the models of *H. dauricus* to species from the three other genera of the Acipenseridae, and other fishes with olfactory rosettes.

2. Materials and methods

Much of the methodology has been described before (Cox, 2008; Abel et al., 2010; Holmes et al., 2011; Rygg et al., 2013; Howard et al., 2013; Ramsey et al., 2015; Agbesi et al., 2016a, 2016b). Therefore, only essential details are given below. Further details are given in Appendix A. Values for the density and dynamic viscosity of (fresh) water given in Sections 2.5.2 and 2.7 were read from Figs. 4.3 and 5.3, respectively, of Denny (1993).

2.1. Specimen

The specimen of *Huso dauricus* used to construct the models is from the Natural History Museum, London, UK, catalogue number BMNH 1925.8.6.2 (Fig. 1). It has a total length of 26 cm (Fig. 1A, *TL*). Based on a) the fact that the 'mean length' of an *H. dauricus* yearling is 35 cm (Berg, 1962) and b) Fig. 5 of Koshelev et al. (2014), the specimen was likely to have been less than one year old when caught, assuming that different populations of *H. dauricus* (Krykhtin and Svirskii, 1997) have similar growth rates (the data of Koshelev et al. relate to specimens of *H. dauricus* from the Amur estuary and lagoon; the Natural History Museum specimen of *H. dauricus* is from the Amur river, precise location unknown). Since capture, the specimen has been stored in 70% industrial methylated spirits, 30% distilled water.

2.2. X-ray micro-computed tomography

X-ray micro-computed tomography (micro-CT) of the head of the specimen of *H. dauricus* was performed at the Henry Moseley X-ray Imaging Facility, University of Manchester, UK, using an XT H 225 system (Nikon Metrology, Tring, UK) equipped with a 22 kV/225 W source and a PerkinElmer XRD 1621 detector. To ensure that the olfactory lamellae were fully separated from each other, as they are likely to be *in vivo*, the specimen was throughout the scan immersed in Fomblin Y04 (Solvay Solexis, Milan, Italy). We have used Fomblin when X-ray scanning and magnetic resonance imaging other fishes (Holmes et al., 2011; Howard et al., 2013). In air, the olfactory lamellae may have adhered to one another (Abel et al., 2010). The voxel size of the scan was 38 μm x 38 μm x 38 μm. The scan comprised the tip of the rostrum to the gill region (Fig. 1A, box). The scan was converted into a set of 1825 TIFF images (e.g. Fig. 2A; [dataset] Garwood et al., 2019) using the software Drishti (Version 2.6.3; Limaye, 2012).

2.3. Surface models

Surface models (Fig. 3) were generated with the software ScanIP (Synopsys, Mountain View, USA). TIFF images from the micro-CT scan were imported into ScanIP. A median filter with a neighbourhood radius of three pixels in the x, y and z directions was applied to the TIFF images to reduce noise and to further improve the contrast between pixels corresponding to the tissue of the specimen and those corresponding to Fomblin (Fig. 2A). The TIFF images were then transformed into a mask of the head (Fig. 2C, Ma) using methodology described previously (Abel et al., 2010; Holmes et al., 2011; Howard et al., 2013; Ramsey et al., 2015; Agbesi et al., 2016a, 2016b). During this process, we removed a barbel that would have obstructed flow into one of the model's nasal chambers (Fig. 3D, black area), and sealed the

mouth (Fig. 3D, white lines). The bent rostral tip (Fig. 1A, asterisk) of the head mask was straightened with the software ZBrush 4R8 (Pixologic, Los Angeles, CA, USA), using the methodology of Agbesi et al. (2016b). The head mask was adjusted to either life-size (for CFD) or three times life-size (for dye visualisation). Surface models of the head (Fig. 3) and the regions corresponding to the plastic model's opaque and translucent parts (Fig. 3C, Op and Tr) were created according to our previous methodology (e.g. Ramsey et al., 2015). The three surface models were then each exported in binary format as stereolithography (STL) files ([dataset] Haysom et al., 2019).

2.4 Plastic model

The plastic model was three times life size a) to better visualise dye behaviour in the nasal region and b) to match the Reynolds number in the dye visualisation experiments to that *in vivo* (Section 2.5.1). The two parts of the plastic model were 3D printed from the corresponding STL files according to the methodology of Abel et al. (2010). The opaque part (Fig. 4A) was made in off-white plastic (ASA, Stratasys, Eden Prairie, USA), giving good contrast with the red dye used to visualise flow; the translucent part (Fig. 4B-D) was made in Accura ClearVue plastic (3D Systems, Rock Hill, South Carolina, USA), facilitating dye visualisation within one of the nasal chambers. The layers arising from the 3D printing process were 178 μm thick in the opaque part and 50 μm thick in the translucent part. To minimise any possible disruption of flow in the nasal region arising from the joint between the two parts, the translucent part included the eye and the entire section of the rostrum (Fig. 4B). The two parts were glued together to give the complete model (Fig. 4). The tips of two barbels were absent from this model (Fig. 4D, circles).

2.5. Fluid dynamics

2.5.1. Dye visualisation

Dye visualisation was performed in an Eidetics Model 1520 closed-circuit, free-surface, continuous-flow flume (Wang et al., 2007) according to our previous methodology (Abel et al., 2010; Agbesi et al., 2016a, 2016b). The working section (L x W x H) of the flume was 152 cm x 38 cm x 51 cm. To obtain a well-defined dye filament, we operated the flume at a free-stream speed (U_0) of 5 cm s^{-1}, corresponding to a Reynolds number of 500 (Section 2.7.2), indicative of laminar flow (Vogel, 1994, pp. 84-85). According to the principle of dynamic similarity (Shapiro, 1961, p. 74; Vogel, 1994, p. 102), a speed of 5 cm s^{-1} with a three times life-size model of *H. dauricus* would correspond to a swimming speed of 15 cm s^{-}

^{1} in the actual specimen, or 0.6 *TL* s^{-1} (*TL* = 26 cm; Section 2.1). Although there is no information on the swimming speed of *H. dauricus*, it is known that sturgeon species belonging to the genus *Acipenser*, which are morphologically similar to *H. dauricus* (cf. Fig. 1A and Fig. A.1A, Appendix A.4), can swim at speeds corresponding to 0.3 – 3 *TL* s^{-1} (4 – 270 cm s^{-1}; e.g. Peake et al., 1997; Wilga and Lauder, 1999; Deslauriers and Kieffer, 2012; Cai et al., 2013; Thiem et al., 2015). Because 0.6 *TL* s^{-1} falls in this range, we considered a Reynolds number of 500 to be physiologically relevant.

The model's pitch (Fig. 4A, Pi) was 0 ± 5°; the limits of this range were similar to the values observed in *Acipenser transmontanus* (Liao and Lauder, 2000). The yaw (Fig. 4D, Ya) was 0 ± 10°, similar to the yaw we observed (Section 2.8) for *Acipenser ruthenus in vivo*. We used one roll value (34°; Fig. 4B, Rl). We visualised flow with red food dye diluted in a ratio of four parts water to one part dye. The dye, as a filament, was directed at the anterior edge of the head (Fig. 4A, arrowhead). The water temperature in the flume varied between 12 – 16.5 °C, and by no more than 2.5 °C in a single day. Dye visualisation experiments were recorded on a Panasonic HC-V500 digital camcorder (50 frames s^{-1}, 1920 pixels x 1080 pixels per frame). Footage was analysed using the software Adobe Premiere Pro CC.

2.5.2. Computational fluid dynamics

The CFD simulation of olfactory flow in *H. dauricus* was performed on a life-sized model derived from the STL model of the head (Section 2.3). A tapered extension ('tail') was added to the back of the STL model using the software GeoMagic Wrap (3D Systems; Appendix A.1.4.2 and A.5, Fig. A.2). We added the tail, which was just over three times the length of the head, to reduce any modification to upstream flow due to the lack of a body (Abel et al., 2010). The STL model ([dataset] Quilter et al., 2019) was converted to a CFD mesh with the snappyHexMesh utility of the software OpenFOAM (Weller et al., 1998). The mesh comprised approximately 63 million cells and was refined in the nasal region (Fig. 5), where the prescribed cell edge length of the surface mesh was 7.8 μm. There were several tens of cells across the centre of each sensory channel (Fig. 5D). Adjacent to the surface of the nasal region, the mesh comprised five layers of cells, each with a prescribed thickness of 2.6 μm (Fig. 5E and F), sufficient to capture the velocity gradients here. The model was placed in a computational domain of dimensions (L x W x H) 30.0 m x 5.6 m x 5.6 m, with a velocity inlet and a pressure outlet. The model lay at the centre of the domain in the transverse plane, with the rostral tip positioned 11.9 m from the velocity inlet. The large size of the computational domain, together with the position of the model within it, were chosen to

minimise flow artifacts from the walls of the domain. Pitch, yaw, and roll were 0°. The density and dynamic viscosity were 999.3 kg m^{-3} and 1.2 x 10^{-3} Pa s, respectively (values for fresh water at 14 °C). The velocity at the inlet was 15 cm s^{-1}, to match the Reynolds number (500) for external olfactory flow in the dye visualisation experiments (Sections 2.5.1 and 2.7.2). The no slip condition was set for all solid surfaces, together with a symmetry plane (with a zero gradient of velocity and pressure across the plane) at the dorsal, ventral, and lateral surfaces of the domain. The ambient static pressure was set to 0. Thus static pressures were gauge pressures (Massey, 1989, p. 6). Flow was assumed to be steady (based on the transient simulation described in Section 2.8), laminar (Section 2.5.1), isothermal, and incompressible. The Navier-Stokes equations governing steady laminar flow were solved with the OpenFOAM algorithm SIMPLEC, giving a field of velocity vectors. Velocities and static pressures were the averages of the last 500 iterations from a total of 2000 iterations of a converged, time-averaged solution to the Navier-Stokes equations. Convergence was checked by monitoring the volumetric flow rate through a plane of refined cells in both the incurrent and the excurrent nostril (e.g. Fig. 5C, arrowheads). Because the volumetric flow rate through this plane changed by ≤ 0.001% over the last 500 iterations of the simulation, we assumed convergence had occurred.

Results from the CFD simulations were analysed and visualised with ParaView (Ayachit, 2016). Full details are given in Appendix A.1.4.2. Static pressures were expressed as pressure coefficients (Vogel, 1988). A pressure coefficient is the ratio of the static pressure (P) to the dynamic pressure (Massey, 1989, p. 98; Vogel, 1994, p. 53) of the free-stream flow ($\frac{1}{2}\rho U_0^2$):

$$C_p = \frac{P}{\frac{1}{2}\rho U_0^2}$$

Equation 1

where ρ is the density of the fluid (999.3 kg m^{-3}, above); U_0 (the free-stream speed) was 15 cm s^{-1}. The difference in static pressure between the incurrent nostril and the excurrent nostril was estimated (Appendix A.1.4.2) by subtracting the average static pressure in the excurrent nostril from the point of maximum static pressure on the wall of the incurrent nostril (Fig. 6B, W).

2.6. Morphometry

Morphometric measurements were made using ParaView, Rhinoceros (Version 4.0, Robert McNeel & Associates), and ScanIP, usually according to previous methodology (Cox, 2008; Abel et al., 2010; Holmes et al., 2011; Cox, 2013; Howard et al., 2013; Ramsey et al., 2015). The inclination of the lateral wall of the incurrent nostril was estimated from the inclination of the incurrent nostril itself to the body axis in lateral profile (Fig. 6A, α). Nasal chamber volumes were estimated according to Appendix A.1.5. Morphometric measurements were made on both the left and right nasal regions.

2.7. Reynolds numbers

2.7.1 General

Reynolds numbers (*Re*) for olfactory flow were calculated using either Equation 2 (Vogel, 1994, p. 85) or Equation 3 (Holmes et al., 2011):

$$Re = \frac{UL\rho}{\mu}$$

Equation 2

$$Re = \frac{4Q\rho}{L\mu}$$

Equation 3

where L is the characteristic dimension of the object, μ is the dynamic viscosity of the fluid, and Q is the volumetric flow rate. Reynolds numbers in the text are given to one significant figure.

2.7.2. Reynolds number for dye visualisation

The Reynolds number for external olfactory flow (i.e. flow over the nasal region) in the plastic model was calculated (Equation 2) with U = 5 cm s^{-1} (the free-stream speed in the flume; Section 2.5.1), L = 12 mm (the width of the nasal region in dorsal profile, perpendicular to the direction of flow; Fig. 4C), and ρ = 998.9 – 999.5 kg m^{-3} and μ = 1.1 – 1.2 x 10^{-3} Pa s at 12 – 16.5 °C (water temperature in the flume; Section 2.5.1).

2.7.3. Reynolds numbers for CFD

Calculations of Reynolds numbers for olfactory flow in the CFD simulation used ρ = 999.3 kg m^{-3} and μ = 1.2 x 10^{-3} Pa s (Section 2.5.2). Reynolds numbers for external olfactory flow were calculated (Equation 2) with U = 15 cm s^{-1} (the free-stream speed in the CFD simulation; Section 2.5.2) and L = 4 mm (Fig. 6C). To calculate Reynolds numbers for flow through the sensory channels, U was measured at the centre of each sensory channel (Fig. 7B, lower inset, disk), and was found to lie in the range 0.4 – 20 mm s^{-1}; L was taken to be the width of the channel at this point (Fig. 7B, lower inset) and was found to lie in the range 100 – 460 μm.

Reynolds numbers for flow through each nasal chamber were calculated (Equation 3; Appendix A.1.6) with Q = 140 – 150 mm^3 s^{-1} (the volumetric flow rate through a sagittal cross-section of the nasal chamber, indicated by line XY in Fig. 6C) and L = 13 mm (the wetted perimeter of that cross-section).

2.8. Data on other sturgeon species

Although not as extensive as the data for *H. dauricus*, we collected data on specimens from the three other extant genera of sturgeons: *Acipenser schrenckii* (anatomical); *A. ruthenus* (anatomical, behavioural); *Pseudoscaphirhynchus kaufmanni* (anatomical, fluid dynamic); and *Scaphirhynchus platorynchus* (anatomical). The (preserved) specimens of *A. schrenckii* (*TL* = 23 cm), *P. kaufmanni* (*TL* = 52 cm) and *S. platorynchus* (*TL* = 54 cm) were from the Natural History Museum, London, UK (catalogue numbers BMNH 1925.8.6.3, 1887.4.5.17, and 1852.8.16.26, respectively; Fig. A.1, Appendix A.4). The (living, freely swimming) specimen of *A. ruthenus* (*TL* ~ 65 cm) was in a public aquarium at Bristol Zoo Gardens, UK.

The data for *A. schrenckii* and *P. kaufmanni* were derived from a micro-CT scan of each specimen (*A. schrenckii* in Fomblin, voxel size 38 μm x 38 μm x 38 μm; *P. kaufmanni* in air, voxel size 69 μm x 69 μm x 69 μm). Each scan was converted to a surface model. The surface model of *P. kaufmanni* was transformed into a plastic model for dye visualisation and a mesh for CFD. The assumption of steady flow in the CFD simulation of *H. dauricus* was based on an initial transient simulation with the *P. kaufmanni* CFD model. In this simulation, the static pressure at a fixed location in the fluid in the incurrent nostril was found over ~ 3.5 s to vary by no more than 0.07% from the equivalent steady-state simulation (Fig. A.3, Appendix A.6). We were able to collect data for external olfactory flow in the *P. kaufmanni* plastic and CFD models, but not for flow in the models' olfactory sensory channels, because the latter were not resolved by the X-ray scan. The surface model of *A. schrenckii* was not of

sufficient quality to transform it into either a plastic or a CFD model (the contrast between Fomblin and the specimen was not as good as in the *H. dauricus* X-ray scan). The data for *A. schrenckii* and *P. kaufmanni* were collected using similar methodology to that described in the previous sections. The data for *A. ruthenus* and *S. platorynchus* were obtained by respectively observing and inspecting each specimen.

2.9. A note on the video clips, figures, and text

For consistency, the video clips (see Video, Supplementary data) and figures are shown in the same orientation, with the anterior part of the head or nasal region to the left. 'Left' and 'Right' labels in the figures refer to, respectively, the left and right nasal regions of the *specimen* of *H. dauricus*, *not* the models (the surface model was reflected during its preparation; Appendix A.1.2). Likewise, any reference to the left or right nasal region in the text (including figure and video clip legends) is always to the left or right nasal region of the *specimen* of *H. dauricus*, not the models. Copyright of the images of the specimens belongs to the Natural History Museum, London, UK.

3. Results

3.1. Nasal anatomy

The paired nasal regions of *Huso dauricus* are located on the dorsal surface of the head (Figs. 1B and 3A-C, NR), away from the mouth, which lies on the ventral surface (Figs. 1G and 3D). Each nasal chamber (Figs. 2B and 4C, NC) is linked to the external environment by two apertures, presumed to be the incurrent nostril and the excurrent nostril (Figs. 1C-F and 6A, IN and EN). The incurrent nostril lies on the dorsoanterior surface of the head (Fig. 6A). It has a broad inner wall (Fig. 6B and C, W). The lateral part of this wall faces anteriorally (Fig. 6B; Fig. 6A and C, arrow 1) and is inclined at an angle of 60 – 70° (Fig. 6A, α). The excurrent nostril faces laterally (Fig. 6B and C, arrow 2). Its aperture is wide, with an area three times larger than the incurrent nostril. The incurrent and excurrent nostrils are separated by a thin flap, referred to here as the nasal bridge (Figs. 1E, 2B and 6A, NB).

Each nasal chamber comprises an olfactory rosette (Figs. 1C, E, 2B, 7B and C) and a relatively large space that connects the incurrent nostril to the excurrent nostril (Fig. 2B, NC). The olfactory rosette is located on the medial wall of the nasal chamber (Fig. 2B, OR), and is made up of an array of olfactory lamellae emanating radially from a circular central support (Figs. 1C, E, 6A, 7B and C, CS). When viewed anterolaterally, the aperture of the incurrent

nostril lies directly above the central support, and is similar in size (Fig. 7A). The lamellae create the olfactory sensory channels (Figs. 1D, F, 2B and 6A, SC). There are 26 sensory channels in the left nasal chamber, and 24 in the right (Fig. 7B and C). Consequently, the nasal chambers are, when considered as a pair, mildly asymmetric. The sensory channels are 1 – 3 mm long, and, at their centres, 0.2 – 1.5 mm deep and 100 – 460 μm wide, with the widths of the channels necessarily increasing distally from the central support (Fig. 7B and C). The variation in sensory channel length makes each olfactory rosette itself asymmetric. With the exception of two sensory channels in the right nasal chamber (Fig. 7B, upper inset), the sensory channels in the surface model were intact. Based on their physical location, and also on flow behaviour in the nasal chamber (Sections 3.2 and 3.3), the sensory channels can be divided into lateral, dorsal, medial, and ventral quadrants (Fig. 7B and C).

The olfactory lamellae are shallow, blade-like structures (Fig. 6A). The dorsal edges of two lamellae in the left nasal chamber were bent in the surface model (Fig. 7C, black disks). Since none of the other lamellae in either the left or the right nasal chamber were bent in this manner, we assume that these two lamellae had become bent well before the X-ray scan (e.g. when the specimen was captured), and not as a result of immersing the specimen in Fomblin for the X-ray scan. Secondary folds are present on the lamellae (just discernible in Fig. 1D, and highlighted by white lines in Fig. 1F) but were not resolved in the X-ray scan, and are therefore not present in the models.

3.2. Dye visualisation

Flow through the nasal chamber of the plastic model of *H. dauricus* was induced by an external flow (Reynolds number 500), with the head either directly facing flow, or with it pitched, or yawed. A dye filament directed at the anterior edge of the head was deflected over the dorsal surface, entered the nasal chamber via the incurrent nostril, and then exited via the excurrent nostril, confirming the roles of these two apertures (Fig. 8A-C, Video clips 1-3). In some instances the dye filament passed through the nasal chamber intact, suggesting a significant pressure difference between the incurrent and excurrent nostrils (Fig. 8D, Video clip 4).

An external flow could also induce flow through the plastic model's sensory channels. (Although the models did not contain any sensory elements, we retain the term 'sensory channels' for consistency.) A dye filament entering the nasal chamber could fan in the vicinity of the central support (Fig. 8E, Video clip 5), indicative of flow decelerating (Shapiro, 1972), and suggesting that the surface of the central support was a region of relatively high static

pressure. The fanning behaviour could result in the passage of dye through the sensory channels in all four quadrants of the olfactory rosette (Fig. 8C and F-K, Video clips 3 and 6-11). We observed dye passing through 15 of the 26 sensory channels in the left nasal region and 11 of the 24 channels in the right nasal region (Fig. 7B and C, yellow disks). We did not observe, or were unable to confirm, dye passage through all of the dorsal sensory channels and seven medial sensory channels (channels 10 – 13, 15, 19 and 20) in the left nasal region, and three dorsal sensory channels (channels 7 – 9) and all of the medial sensory channels in the right nasal region. We failed to do so either because it was difficult to orientate the model to see these channels, or because of the plastic model's opacity. Dye passed through the sensory channels from the central support to the periphery of the olfactory rosette (e.g. Fig. 8C).

Dye behaved in the nasal chamber according to where it entered the incurrent nostril. Dye passage through the sensory channels occurred when the filament entered the central, medial, or dorsal parts of the incurrent nostril, specifically: central incurrent nostril → lateral sensory channels (e.g. Fig. 8F, Video clip 6); dorsal incurrent nostril → dorsal sensory channels (Fig. 8K, Video clip 11); dorsomedial incurrent nostril → medial sensory channels (Fig. 8J, Video clip 10); and ventromedial incurrent nostril → ventral sensory channels (Fig. 8G, Video clip 7). Dye entering the dorsomedial or ventral parts of the incurrent nostril resulted in vortical structures (V1-3, Fig. 8L and M, Video clips 12 and 13; Lugt, 1983; Agbesi et al., 2016a; for brevity, hereafter we use the terms 'vortices' or 'vortex').

3.3. Computational fluid dynamics

Using the same Reynolds number (500) as for dye visualisation, olfactory flow in *H. dauricus* was investigated by CFD, with the head directly facing flow (pitch, yaw, and roll 0°). The results from the CFD simulation were consistent with the dye visualisation experiments, indicating that the CFD results were valid. Thus, the behaviour of dye in the plastic model in the flume could be replicated by streamlines generated from the CFD simulation (Fig. 9). For example, dye behaviour in Video clip 4 (Fig. 8D) could be replicated by the streamline shown in Fig. 9A, and vortices V1-3 in Video clips 12 and 13 (Fig. 8L and M) could be replicated by the streamlines shown in Fig. 9B and C. In addition, streamlines that passed through the sensory channels entered the incurrent nostril at similar points to the dye filament (Fig. 10A-D; Section 3.2). The CFD simulation also showed that, as suggested by the dye visualisation experiments: a) there was a significant pressure difference between the incurrent nostril and the excurrent nostril: 10 Pa, ~ 90% of the dynamic pressure of the free-stream flow (Section 2.5.2); b) the surface of the olfactory rosette's central support was a region of

relatively high static pressure (Figs. 11C and 12); and c) flow decelerated as it approached the central support (Fig. 13).

Additionally, the CFD simulation showed that: a) the model's stagnation point was located on the rostral tip (Fig. 11A, disk); b) the lateral wall of the incurrent nostril was also a region of particularly high static pressure (Fig. 11B); c) streamlines passing through the sensory channels had a relatively high speed (> 8 cm s^{-1}) when they passed through the incurrent nostril (Fig. 10E); d) these streamlines impinged on the region of relatively high static pressure on the olfactory rosette's central support (Fig. 12); e) vortices V1 and V2 arose from streamlines passing through the dorsal and medial sensory channels, respectively (Fig. 12B and C); f) streamlines passing through some medial and ventral sensory channels (channels 21 and 24 in the left nasal chamber, 17 – 21 in the right) produced a vortex *within* these sensory channels (e.g. Fig. 12C, V4); g) the volumetric flow rate through the nasal chamber was 140 – 150 mm^3 s^{-1} (~ two nasal chamber volumes s^{-1}; the volume of the nasal chamber was 70 mm^3); and h) the Reynolds number for flow through the nasal chamber was 40. Reynolds numbers for flow through the sensory channels ranged from 0.1 to 8.

4. Discussion

4.1. Flow through the nasal chamber is induced by an external flow

We showed that flow through the nasal chamber of a model of the sturgeon *Huso dauricus* can be induced by an external flow at a physiologically relevant Reynolds number (500). *In vivo*, the origin of this external flow would almost certainly be *H. dauricus*'s own movement as it swims forward, given that it is a highly active swimmer (Vecsei and Peterson, 2004). An oncoming environmental (e.g. riverine) current could contribute further to external flow.

The pressure difference driving flow through the nasal chamber of *H. dauricus* may be attributed to three sources:

a) The distribution of static pressure on the surface of the head. The incurrent nostril is located in a region of high static pressure ($Cp > 0$; Fig. 11), caused by the inclined dorsoanterior surface of the head impeding flow. The lateral wall of the incurrent nostril, which faces oncoming flow (Fig. 11B), is a region of particularly high static pressure, with *Cp* rising to > 0.99 (Fig. 11B, disk). The lateral wall is supported by a cartilaginous bar (Fig. 11B, CB), which may help it withstand the relatively high pressures to which it is exposed (Vogel, 1988). The excurrent

nostril, on the other hand, is located on the lateral surface of the head, in a region of low static pressure ($Cp < 0$; Fig. 11C), caused by flow accelerating around the nasal region. As a result of the distribution of static pressure on the surface of the head, there will be a tendency for flow to be forced into the incurrent nostril and to be drawn out of the excurrent nostril. Vogel (1988) has made this point previously in respect to the nasal regions of fishes.

b) The excurrent nostril is roughly perpendicular to oncoming flow (Fig. 11B). The fluid within it should therefore experience only the ambient static pressure of the fluid. This proved to be nearly the case in the CFD simulation, where the average static pressure of the fluid in the excurrent nostril was 1 Pa (ambient static pressure = 0), 9% of the dynamic pressure of the free stream flow (Section 2.5.2).

c) Viscous entrainment (Cox, 2008). Water flowing over the relatively wide excurrent nostril should entrain fluid from this nostril.

Thus, the overall pressure difference driving flow through *H. dauricus*'s nasal chamber arises from the position and orientation of the incurrent and excurrent nostrils on the surface of the head, probably in conjunction with entrainment from the excurrent nostril. External flow is captured very efficiently by this anatomical arrangement (~ 90% of the dynamic pressure of the free stream is harnessed).

4.2. Flow through the olfactory sensory channels is induced by an external flow

Crucially, we showed that an external flow also induced flow through the olfactory sensory channels of the *H. dauricus* plastic model. In the dye visualisation experiments, we observed flow through about half (15/26) of the sensory channels in the left nasal region, and about half (11/24) in the right nasal region (Fig. 7B and C). The remaining sensory channels were located in the dorsal and medial quadrants of the olfactory rosette, which were difficult to see in the plastic model. We were able, however, to infer from the CFD simulation that flow had probably occurred through some of the obscured channels. Thus CFD-generated streamlines in the obscured channels of the left nasal chamber recreated two of the vortices observed in the dye visualisation experiments (Fig. 8L, V1 and V2; Video clip 12): streamlines passing through dorsal sensory channels 7 and 8 recreated vortex V1 and streamlines passing through medial sensory channels 10 – 16 recreated vortex V2 (Fig. 9B). The agreement between the CFD-generated streamlines and dye behaviour suggests that flow did in fact occur through sensory channels 7, 8, 10 – 13 and 15, although we did not observe it directly. In other words,

vortices V1 and V2 in Fig. 8L/Video clip 12 are indicative of flow through seven additional sensory channels in the left nasal chamber (Fig. 7C, red disks). Therefore, dye may have passed through up to 22 of the 26 sensory channels in the left nasal chamber.

Our results suggest that flow is driven through the sensory channels by the following mechanism. Relatively high speed (and therefore high momentum) flow passing through the incurrent nostril (Fig. 10E) strikes the broad surface of the olfactory rosette's central support, decelerates, and as a result fans across the edge of the central support and into the sensory channels (Fig. 13). The central support therefore has both a structural function (supporting the olfactory lamellae) and a hydrodynamic function (dispersing flow over the olfactory sensory surface). The interaction between incurrent flow and the central support is facilitated by the position of the incurrent nostril over the central support (at least in an anterolateral view; Fig. 7A and B). This interaction is also facilitated by the wall of the incurrent nostril, which guides flow onto the central support. The arrangement of the incurrent nostril and the central support is not unlike an impingement jet for heat and mass transfer in engineering (Incropera et al., 2013, pp. 477 - 482), where the jet spreads over the surface it strikes rather than rebounding from it (Massey, 1989, p. 117). The widening olfactory sensory channels may act as diffusers, reducing energy losses (Massey, 1989, pp. 212-214). Odorant transport within the sensory channels occurs in a laminar regime, with Reynolds numbers in the range 0.1 – 8 (i.e. inertial and viscous forces are finely balanced; Shapiro, 1961, p. 78), similar to Reynolds numbers in the sensory channels of other fishes (0.02 – 5; Cox, 2008; Holmes et al., 2011).

4.3. Other mechanisms that may assist olfactory flow

We cannot rule out the possibility that the beating cilia of the many non-sensory ciliated cells lining the sensory olfactory epithelium of a sturgeon (e.g. Fig. 2 of Camacho et al., 2010) assist olfactory flow, because our inanimate model did not take into account the action of these cells. Non-sensory ciliated cells in the olfactory epithelia of fishes have been shown either directly (Reiten et al., 2017) or indirectly (e.g. Teichmann, 1959) to generate water currents, although these cells may also propel mucus (Cox, 2013). Respiration, on the other hand, is not likely to assist olfactory flow in *H. dauricus*, because its mouth is located on the ventral surface of its body (Fig. 1G). Indeed, the movements of the mouth that we observed during normal respiration in *Acipenser ruthenus in vivo* were slight (Fig. 1G, asterisk), suggesting that their influence would not extend to the nasal region.

539 *4.4. Vortices*

540 We identified several vortices in the internal olfactory flow of *H. dauricus*, either in the
541 relatively large space connecting the incurrent nostril to the excurrent nostril (Fig. 8L and M,
542 V1-3), or within some of the medial and ventral sensory channels (e.g. Fig. 12C, V4). The
543 vortices could have two beneficial effects on odorant transport. First, V1 could drive flow into
544 the lateral sensory channels (Fig. 12B, dashed line through lateral sensory channel 3), thereby
545 assisting convective odorant transport to these channels. Similarly, V2 could draw flow *out* of
546 the ventral sensory channels (Fig. 12C, dashed line through ventral sensory channel 23).
547 Second, V4 could assist diffusive odorant transport by creating a relatively steep velocity
548 gradient (Bashor et al., 1974; Vogel, 1994, p. 212 and pp. 355-356). The presence of vortices
549 in the nasal chamber of *H. dauricus* supports the notion that they are not uncommon elements
550 in ichthyic olfactory flow (Agbesi et al., 2016b). The vortices observed here, however, occurred
551 at lower Reynolds numbers (0.1 – 8 and 40) than the ones observed previously (700 – 5,000;
552 Agbesi et al., 2016a, 2016b).

553

554 *4.5. Implications for olfactory flow in other sturgeons and other fishes*

555 The nasal anatomy of the preserved specimens from the three other extant genera of sturgeons
556 (*Acipenser*, *Pseudoscaphirhynchus* and *Scaphirhynchus*) that we inspected was similar to that
557 of *H. dauricus*. They all had: a) olfactory rosettes comprising ~ 20 – 25 sensory channels (cf.
558 19 – 32 sensory channels in the olfactory rosettes of other species of *Acipenser* and
559 *Scaphirhynchus*: Fig. 1 of Pyatkina, 1975; Table 2 of Chen and Arratia, 1994; Fig. 2 of
560 Camacho et al., 2010); b) similar narial arrangements (this was also true of *A. ruthenus in vivo*),
561 with the incurrent nostril on the dorsoanterior surface of the nasal region, and the excurrent
562 nostril on the lateral surface of the head, roughly perpendicular to oncoming flow (Figs. 14 and
563 15); and c) an incurrent nostril with a broad inner wall, the lateral part of which faced
564 anteriorally (Figs. 14C, 15C and D). Furthermore, inspection of the X-ray scans of *Acipenser*
565 *schrenckii* and *Pseudoscaphirhynchus kaufmanni* showed that, as in *H. dauricus*, the lateral
566 part of the incurrent nostril wall in these two species is supported by a cartilaginous bar. We
567 were able to visualise the cartilaginous bar *in situ* in the surface model of *P. kaufmanni* (Fig.
568 14C, CB). Also as in *H. dauricus*, the incurrent nostril of both *A. schrenckii* and *P. kaufmanni*
569 is positioned over the olfactory rosette's central support in an anterolateral view (Figs. 14C,
570 inset, and 15B). Finally, like *H. dauricus*, the number of sensory channels in *A. schrenckii* was,
571 as determined from the surface model, mildly asymmetric (26 in the left nasal chamber, 24 in
572 the right), so such asymmetry may be common in sturgeons.

573

Given these anatomical similarities, we expect olfactory flow in other sturgeons to be very similar to that in the *H. dauricus* models, with external flow driving flow through the nasal chamber and olfactory sensory channels, and the presence of vortices in the nasal chamber. Indeed, we have shown in a plastic model of *P. kaufmanni* that flow through the nasal chamber *is* driven by an external flow (Video clip 14), and in both a plastic and a CFD model of *P. kaufmanni* that vortices *did* occur in the nasal chamber (Fig. 16; Video clip 15). The externally-induced olfactory flow and the vortices in the *P. kaufmanni* models both occurred at Reynolds numbers (700 and 20, respectively) similar to those in the *H. dauricus* models (500 and 40, respectively). We were unable, however, to determine whether external flow can drive flow through the olfactory sensory channels of *P. kaufmanni*, because these channels were not resolved in the plastic or the CFD model of this specimen.

We observed two variable features in the nasal anatomy of the sturgeon. The first was the inclination of the lateral wall of the incurrent nostril (Fig. 6A, α). In *Acipenser* and *Huso*, the inclination was quite steep (α = 50 – 75°). In *Pseudoscaphirhynchus* and *Scaphirhynchus*, which have flattened rostra (e.g. Fig. 14B), the inclination was less (α = 35 – 50°). We would expect external flow to be captured more efficiently at greater inclinations, because the obstruction to flow will be greater, and therefore the pressure coefficient on the incurrent nostril wall will be greater. This did indeed seem to be true in the CFD simulations for *H. dauricus* and *P. kaufmanni* (90% of the dynamic pressure available from the external flow is harnessed in *H. dauricus* v. 70 – 80% in *P. kaufmanni*). The second variable anatomical feature was the anterior edge of the excurrent nostril, which was raised in *A. schrenckii* (Fig. 15A-C), but not in the other specimens. The raised edge should, by acting as a bluff body, reduce further the static pressure at the excurrent nostril (Douglas et al., 1985, p. 296), and therefore lead to more efficient capture of external flow.

Other fishes apart from sturgeons have well-developed olfactory rosettes, including *Aphanopus carbo* (Trichiuridae; Holl and Meinel, 1968), chimaeras (Chimaeridae; Howard et al., 2013), and cow sharks (Hexanchidae; Meng and Yin, 1981; Ferrando et al., 2017). The number of sensory channels in the olfactory rosettes of these fishes (18 – 36) is similar to that in sturgeons. In addition, like sturgeons, the incurrent nostrils of *Aphanopus carbo* and chimaeras are known to be situated over the olfactory rosette's central support (Fig. 2 of Holl and Meinel, 1968; Fig. 11 of Howard et al., 2013). Furthermore, the relatively long incurrent channel of chimaeras, together with its nozzle-like exit, appears set up to direct a stream of fluid onto the central support (Fig. 9F and G of Howard et al., 2013). Flow through the nasal chambers of these fishes

609 is, however, generated by different (inferred) pumps: accessory sacs (*Aphanopus carbo*);
610 respiration (chimaeras); and swimming (cow sharks). But because these fishes have olfactory
611 rosettes that are similar to those of sturgeons, we suggest that the different pumps all perform
612 the same function. Thus each type of pump is likely to drive flow onto the central support,
613 where it then decelerates and is dispersed amongst the sensory channels. In other words, it is
614 likely that flow can be driven through the sensory channels of an olfactory rosette by the action
615 of a *single* pump, although the nature of that pump (accessory sacs, respiration, swimming) can
616 vary.
617
618 *4.6. Limitations*
619 The dye visualisation experiments involving the plastic model of *H. dauricus* were limited in
620 several ways. a) The model lacked a body. The resultant abrupt change in geometry at the back
621 of the head caused flow to separate at this point (Video clip 16), which may have modified
622 upstream flow (e.g. in the nasal region). b) The model bears fine ridges (178 μm thick in the
623 opaque part and 50 μm thick in the translucent part) arising from the 3D printing process, which
624 builds the models in layers (Section 2.4). c) The edge of the excurrent nostril in the opaque
625 nasal region is not as smooth as it is in the specimen (cf. Video clip 5 and Fig. 1D), another
626 consequence of the resolution of the 3D printing process. Because the model was three times
627 life-size, its effective resolution was three times the resolution of the X-ray scan (38 μm), i.e.
628 114 μm. Thus the 178 μm thick ridges in the model's opaque part would have lost some of the
629 detail of the X-ray scan. d) The walls of the flume could have affected olfactory flow in the
630 model.
631
632 Each of the above limitations was addressed by the CFD simulation, where: a) the model bore
633 a tapered extension to prevent flow separating from its posterior surface (Fig. A.2, Appendix
634 A.5); b) the surface of the model was smooth; c) the edge of the excurrent nostril was faithfully
635 reproduced (Fig. 5A); d) the distance between the model and the walls of the computational
636 domain was substantial (~ 2.8 m; in the flume it was ≥ 14 cm). Given that olfactory flow in the
637 dye visualisation experiments was similar to that in the CFD simulation, we conclude that the
638 limitations of the dye visualisation experiments did not significantly affect olfactory flow in
639 the plastic model.
640
641 There were several limitations that we did not address in the *H. dauricus* models. a) We
642 assumed that the sturgeon's olfactory lamellae were unlikely to be deflected by water flowing
643 over or between them. Although we attempted to verify this assumption by observing the nasal

region of *A. ruthenus in vivo*, the continuous movement of the fish meant that we were unable to do so. b) Whilst the secondary folds were present in the preserved specimen (Fig. 1D and F), they were not resolved in the X-ray scan of *H. dauricus*, and so were not present in our models. We could not therefore observe their hydrodynamic effect. A higher resolution micro-CT scan may in the future allow one to do so, e.g. by CFD. c) There were two small gaps between the olfactory lamellae and the central support in the right nasal chamber (Fig. 7B, upper inset, disks). d) The dorsal edges of two olfactory lamellae in the left nasal region were bent (Fig. 7C, black disks). e) Prior to the X-ray scan, the *H. dauricus* specimen is likely to have undergone some shrinkage during its (~ 90 years) period of storage in alcoholic preservative (Abel et al., 2010). f) *In vivo*, as we observed in *A. ruthenus*, the eyes of a sturgeon are convex. The eyes of the preserved specimen of *H. dauricus* used to construct our models had, however, collapsed to a flattened state (similar to Fig. 15B). g) The barbels in the models were either truncated or flattened against the body (Figs. 3D and 4D). *In vivo*, based on our aquarium observations of *A. ruthenus*, the barbels are likely to be extended ventrally (Fig. 1G). h) Flow was steady in our experiments. *In vivo*, flow is likely to be both steady (e.g. when the sturgeon is cruising) and unsteady (e.g. when the sturgeon is turning). i) We did not investigate the effect the substrate has on olfactory flow. In our experiments, the ventral surface of each model was placed well away from the substrate. *In vivo*, sturgeons typically swim close to the substrate (Vecsei and Peterson, 2004). The aquarium specimen of *A. ruthenus* could, however, swim well above the substrate. *H. dauricus*, as a highly active swimmer (Vecsei and Peterson, 2004), may also swim well above the substrate.

Although some of these limitations may have modified olfactory flow, given the sensory channels were generally fully formed, and the nasal anatomy of *H. dauricus* was very similar to that of *A. ruthenus in vivo*, the extent of the modification is unlikely to have been great. Consequently, we believe that olfactory flow in the models of *H. dauricus* is a fairly accurate reflection of olfactory flow *in vivo*.

5. Conclusion

An external flow alone is sufficient to drive water through both the nasal chamber and the olfactory sensory channels of a sturgeon. The arrangement of the incurrent and excurrent nostrils on the surface of the head causes the pressure difference that drives flow through the nasal chamber, whilst the central support of the olfactory rosette is responsible for dispersing flow amongst the sensory channels. The wall of the incurrent nostril is instrumental in both

processes. This study is we believe the first physical demonstration of externally induced flow through the olfactory sensory channels of a fish.

Acknowledgements

We thank Laser Lines/Ogle Models and Prototypes for 3D printing, Matt Cross, Paul Frith, Mary Mahon, George Oates, Ian Trussler, Zhijin Wang, and Simon Wharf for technical assistance, Ismet Gursul and Richie Gill for allowing us to use, respectively, the flume and ScanIP software in the Department of Mechanical Engineering at Bath, Kevin Webb and Nic Delves-Broughton for photography, David Cleaver for helpful discussions, Dan Sykes and Mawuli Agbesi for contributing to the work on *Pseudoscaphirhynchus kaufmanni* (X-ray scan and dye visualisation, respectively), Xavier Mear for German to English translation, and Olivia Edgar for facilitating the observations of *Acipenser ruthenus* at Bristol Zoo Gardens, UK.

Funding statement

This work was supported by the University of Bath's Alumni Fund. The Engineering and Physical Sciences Research Council, UK, funded the Henry Moseley X-ray Imaging Facility through the Royce Institute for Advanced Materials (grants EP/F007906/1, EP/F001452/1, EP/I02249X, EP/M010619/1, EP/F028431/1, EP/M022498/1 and EP/R00661X/1). The funding sources had no involvement in the conduct of the research, or the preparation of the article.

References

Abel, R.L., Maclaine, J.S., Cotton, R., Xuan, V.B., Nickels, T.B., Clark, T.H., Wang, Z., Cox, J.P.L., 2010. Functional morphology of the nasal region of a hammerhead shark. Comp. Biochem. Physiol. A 155, 464-475.

Agbesi, M.P.K., Naylor, S., Perkins, E., Borsuk, H.S., Sykes, D., Maclaine, J.S., Wang, Z., Cox, J.P.L., 2016a. Complex flow in the nasal region of guitarfishes. Comp. Biochem. Physiol. A 193, 52-63.

Agbesi, M.P.K., Borsuk, H.S., Hunt, J.N., Maclaine, J.S., Abel, R.L., Sykes, D., Ramsey A.T., Wang, Z., Cox, J.P.L., 2016b. Motion-driven flow in an unusual piscine nasal region. Zoology 119, 500-510.

Ayachit, U., 2016. The *ParaView Guide*. Kitware Inc.

Bashor, D.P., Beuerman, R.W., Easton, D.M., 1974. Ciliary action and normal movement of odorant wavefronts in garfish nasal capsule of *Lepisosteus osseus*. Experientia, 30, 777-779.

Berg, L.S., 1962. Freshwater fishes of the U.S.S.R and adjacent countries. Israel Program for Scientific Translations, Jerusalem.

Cai, L., Taupier, R., Johnson, D., Tu, Z., Liu, G., Huang, Y., 2013. Swimming capability and swimming behavior of juvenile *Acipenser schrenckii*. J. Exp. Zool. 319A, 149-155.

Camacho, S., Ostos-Garrido, M.V., Domezain, A., Carmona, R., 2010. Study of the olfactory epithelium in the developing sturgeon. Characterization of the crypt cells. Chem. Senses. 35, 147-156.

Chen, X.-Y., Arratia, G., 1994. Olfactory organ of Acipenseriformes and comparison with other Actinopterygians. J. Morph. 222, 241-267.

Cox, J.P.L., 2008. Hydrodynamic aspects of fish olfaction. J. Roy. Soc. Interface 5, 575-593.

Cox, J.P.L., 2013. Ciliary function in the olfactory organs of sharks and rays. Fish and Fish. 14, 364-390.

Denny, M.W., 1993. Air and Water. Princeton University Press, Princeton.

Deslauriers, D., Kieffer, J.D., 2012. The effects of temperature on swimming performance of juvenile shortnose sturgeon (*Acipenser brevirostrum*). J. Appl. Ichthyol. 28, 176-181.

726 Devitsyna, G.V., Kazhlayev, A.A., 1992. Development of chemosensory organs in the
727 Siberian sturgeon *Acipeser baerii* and stellate sturgeon A. *stellatus*. Vopr. Ikhtiol. 32, 167-
728 175.

729 Douglas, J.F., Gasiorek, J.M., Swaffield, J.A., 1985. Fluid Mechanics. 2nd ed. Pitman,
730 Massachusetts.

731 Ferrando, S., Gallus, L., Amaroli, A., Gambardella, C., Waryani, B., Di Blasi, D., Vacchi,
732 M., 2017. Gross anatomy and histology of the olfactory rosette of the shark *Heptranchias*
733 *perlo*. Zoology 122, 27-37.

734 Garwood, R.J., Behnsen, J., Maclaine, J.S., Cox, J.P.L., 2019. TIFF images from X-ray scan of
735 *Huso dauricus*. Mendeley Data. (Final link not yet available.)

736 Hansen, A., Zielinski, B.S., 2005. Diversity in the olfactory epithelium of bony fishes:
737 development, lamellar arrangement, sensory neuron types and transduction components. J.
738 Neurocytol., 34, 183-208.

739 Haysom, H.K., Hunt, J.N., Cox, J.P.L., 2019. STL model of head of *Huso dauricus*.
740 Mendeley Data. (Final link not yet available.)

741 Holl, A., Meinel, W., 1968. The olfactory organ of the deep-sea fish *Aphanopus carbo*
742 (Percomorphi, Trichiuridae). Helgoländer wiss. Meeresunters. 18, 404-423. In German, with
743 an English summary.

744 Holmes, W.M., Cotton, R., Xuan, V.B., Rygg, A.D., Craven, B.A., Abel, R.L., Slack, R.,
745 Cox, J.P.L., 2011. Three-dimensional structure of the nasal passageway of a hagfish and its
746 implications for olfaction. Anat. Rec. 294, 1045-1056.

747 Howard, L.E., Holmes, W.M., Ferrando, S., Maclaine, J.S., Kelsh, R.N., Ramsey, A., Abel,
748 R.L., Cox, J.P.L., 2013. Functional nasal morphology of chimaerid fishes. J. Morph. 274,
749 987-1009.

750 Incropera. F.P., Dewitt, D.P., Bergman, T.L., Lavine, A.S., 2013. Principles of Heat and
751 Mass Transfer. 7th ed. John Wiley & Sons, Singapore.

752 Kasumyan, A.O., 2004. The olfactory system in fish: structure, function, and role in behavior.
753 J. Ichthyol. 44, S180-S223.

754 Koshelev, V.N., Mikheev, P.B., Shmigirilov, A.P., 2014. Age and growth of kaluga
755 *Acipenser dauricus* from the estuary of the Amur and its lagoon. J. Ichthyol. 54, 165-176.

Krykhtin, M.L., Svirskii, V.G., 1997. Endemic sturgeons of the Amur River: kaluga, *Huso dauricus*, and Amur sturgeon, *Acipenser schrenckii*. Environ. Biol. Fishes 48, 231-239.

Liao, J., Lauder, G.V., 2000. Function of the heterocercal tail in white sturgeon: flow visualization during steady swimming and vertical maneuvering. J. Exp. Biol. 203, 3585-3594.

Lim, T.T., 2000. Dye and smoke visualization. In: Smits, A.J., Lim, T.T. (Eds.), Flow Visualization. Imperial College Press, London, pp. 43-72.

Limaye, A., 2012. Drishti: a volume exploration and presentation tool. In: Stock, S.R. (Ed.), Proceedings SPIE 8506, Developments in X-ray Tomography VIII, 85060X.

Lugt, H.J., 1983. Vortex Flow in Nature and Technology. John Wiley & Sons, New York.

Massey, B.S., 1989. Mechanics of Fluids, 6th ed. Van Nostrand Reinhold, London.

Meng, Q., Yin, M., 1981. A study of the olfactory organ of the sharks. Trans. Chinese Ichthyol. Soc. 2, 1-24. In Chinese, with an English summary.

Nelson, J.S., 2006. Fishes of the World. 4th ed. John Wiley & Sons, New Jersey.

Peake, S., Beamish, F.W.H., McKinley, R.S., Scruton, D.A., Katopodis, C., 1997. Relating swimming performance of lake sturgeon, *Acipenser fulvescens*, to fishway design. Can. J. Fish. Aquat. Sci. 54, 1361-1366.

Pyatkina, G.A., 1975. Electron microscopic study of the olfactory organ in the sterlet *Acipenser ruthenus*. Arch. Anat. Gistol. Embriol. 68, 85-93. In Russian, with an English summary.

Quilter, S.K., Dalby, L.J., Cox, J.P.L., 2019. STL model of head of *Huso dauricus*, with tapered extension. Mendeley Data. (Final link not yet available.)

Ramsey, A., Houston, T.F., Ball, A.D., Goral, T., Barclay, M.V.L., Cox, J.P.L., 2015. Towards an understanding of molecule capture by the antennae of male beetles belonging to the genus *Rhipicera* (Coleoptera, Rhipiceridae). Anat. Rec. 298, 1519-1534.

Reiten, I., Uslu, F.E., Fore, S., Pelgrims, R., Ringers, C., Verdugo, C.D., Hoffman, M., Lal, P., Kawakami, K., Pekkan, K., Yaksi, E., Jurisch-Yaksi, N., 2017. Motile-cilia-mediated flow improves sensitivity and temporal resolution of olfactory computations. Curr. Biol. 27, 166-174.

785 Rygg, A.D., Cox, J.P.L., Abel, R., Webb, A.G., Smith, N.B., Craven, B.A., 2013. A
786 computational study of the hydrodynamics in the nasal region of a hammerhead shark
787 (*Sphyrna tudes*): implications for olfaction. PLOS ONE 8, e59783, 1-19.

788 Settles, G.S., 2005. Sniffers: fluid-dynamic sampling for olfactory trace detection in Nature
789 and homeland security. J. Fluids Eng. 127, 189-218.

790 Shapiro, A.H., 1961. Shape and Flow. Heinemann, London.

791 Shapiro, A.H., 1972. Pressure fields and fluid acceleration. In: National Committee for Fluid
792 Mechanics Films, Illustrated Experiments in Fluid Mechanics. MIT Press, London, pp 39-46.

793 Teichmann, H., 1959. Über die Leistung des Geruchssinnes beim Aal [*Anguilla anguilla* (L.)]
794 (On the performance of the sense of smell of the eel). Z. vgl. Physiol. 42, 206-254. In German.

795 Thiem, J.D., Dawson, J.W., Gleiss, A.C., Martins, E.G., Haro, A., Castro-Santos, T.,
796 Danylchuk, A.J., Wilson, R.P., Cooke, S.J., 2015. Accelerometer-derived activity correlates
797 with volitional swimming speed in lake sturgeon (*Acipenser fulvescens*). Can. J. Zool. 93,
798 645-654.

799 Tu, J., Yeoh, G.-H., Liu, C., 2018. Computational Fluid Dynamics. 3rd ed. Butterworth-
800 Heinemann, Oxford.

801 Vecsei, P., Peterson, D., 2004. Sturgeon ecomorphology: a descriptive approach. In:
802 LeBreton, G.T.O., Beamish, F.W.H., McKinley, R.S. (Eds.), Sturgeons and Paddlefish of
803 North America. Kluwer Academic Publishers, Dordrecht, pp. 103-133.

804 Vogel, S., 1988. How organisms use flow-induced pressures. Am. Sci. 76, 28-34.

805 Vogel, S., 1994. Life in Moving Fluids. 2nd ed. Princeton University Press, Princeton.

806 Wang, Z.-J., Jiang, P., Gursul, I., 2007. Effect of thrust-vectoring jets on delta wing
807 aerodynamics. J. Aircraft 44, 1877-1888.

808 Weller, H.G., Tabor, G., Jasak, H., Fureby, C., 1998. A tensorial approach to computational
809 continuum mechanics using object-oriented techniques. Comp. Phys. 12, 620-631.

810 Wilga C.D., Lauder, G.V., 1999. Locomotion in sturgeon: function of the pectoral fins. J.
811 Exp. Biol. 202, 2413-2432.

812 Zeiske, E., Kasumyan, A., Bartsch, P., Hansen, A., 2003. Early development of the olfactory
813 organ in sturgeons of the genus *Acipenser*: a comparative and electron microscopic study.
814 Anat. Embryol. 206, 357-372.

Figure legends

Fig. 1 Specimen of *Huso dauricus* (BMNH 1925.8.6.2) used to generate the models for fluid dynamics. (A) Right side of specimen (photograph flipped horizontally). Box: extent of X-ray scan. Asterisk: bent rostral tip. (B) Lateroventral aspect of head. (C) and (E): Left nasal region. (D) and (F): right nasal region. Important nasal features are highlighted by continuous or dashed lines in (E) and (F). (G) Ventral aspect of head and outline of lateral aspect of head showing extent of mouth opening during regular respiration (asterisk) and typical position of barbels when swimming, based on our observations of *Acipenser ruthenus in vivo*. Image flipped vertically, to match Figs. 3D and 4D. Ba: Barbel; CS: central support; EN: excurrent nostril; Ey: eye; He: head; IN: incurrent nostril; La: olfactory lamella; Mo: mouth; NB: nasal bridge; NR: nasal region; SC: sensory channel; SF: secondary fold; *TL*: total length.

Fig. 2 Image processing. (A) TIFF image from micro-CT scan of *Huso dauricus*. Transverse cross-section through head. Inset: right lateral aspect of head of specimen, indicating location of cross-section (dashed vertical line). Inset image flipped horizontally. (B) Same image after application of median filter. Cartilaginous bars, nasal chamber wall, olfactory rosette, and a sensory channel highlighted in yellow. (C) Same image as (B) with mask superimposed. Scale bar applies to all three images. Ba: Barbel; Ca: cartilage; CB: cartilaginous bar; d: dorsal; Fo: Fomblin; IN: incurrent nostril; La: olfactory lamella; Ma: mask; NB: nasal bridge; NC: nasal chamber; OR: olfactory rosette; SC: sensory channel; Ti: tissue; v: ventral; W: incurrent nostril wall.

Fig. 3 Surface model of *Huso dauricus*. (A) Lateral aspect. (B) Anterior and anterolateral aspects. (C) Dorsal aspect. (D) Ventral aspect. White lines: filled regions. Black area: base of removed barbel. White areas: barbel tips absent in plastic model. Ba: Barbel; EN: excurrent nostril; IN: incurrent nostril; Mo: mouth; NR: nasal region; Op: opaque and Tr: translucent parts in plastic model, respectively.

Fig. 4 Plastic model of *Huso dauricus*. (A) Lateral aspect of opaque nasal region. (B) Lateral aspect of translucent nasal region (image flipped horizontally). X, Y and Z: faces of flume. Eyes and arrows indicate observer's viewpoint. Circular symbol indicates free-stream flow towards reader. I, II, III: model orientations in flume (upright, upside down, and rolled, respectively). (C) Dorsal aspect. Box: detail of opaque nasal region. Asterisk: hole for fixing model upright or upside down in flume. (D) Ventral aspect. Circles: missing barbel tips. White area: base of removed barbel. Lines: filled regions. Images above model in (A) – (C): posterior

region of model, highlighting aluminium peg. Arrowhead in (A): area at which dye filament directed. Scale bar in (A) applies to all images. Ba: Barbel; EN: excurrent nostril; Ey: eye; FW: outline of flume walls (not to scale); IN: incurrent nostril; *L*: characteristic dimension of nasal region; Mo: mouth; NC: nasal chamber; Op: opaque part; Pe: aluminium peg; Pi: pitch; Rl: roll; Tr: translucent part; Ya: yaw.

Fig. 5 CFD mesh of *Huso dauricus*. (A) Refinement of mesh on model surface, corresponding to right nasal region of specimen. Large circles: enlargements of points (small circles) at three stages of refinement, with refinement increasing right to left. (B) Mesh representing fluid surrounding cross-section of model head (same cross-section as in Fig. 2). (C) Cross-section through right nasal region. Arrowheads: plane of refined cells for monitoring volumetric flow rate through incurrent nostril. Disks: edge of incurrent nostril. (D) Cross-section through an olfactory sensory channel. (E) Mesh representing fluid adjacent to olfactory lamellar surface. (F) The five layers of refined cells (shaded) immediately adjacent to lamellar surface. (E) and (F) redrawn for clarity. Labels in (A) and scale bars in (A) – (E) deliberately omitted to allow reader to see mesh. d: Dorsal; La: olfactory lamella; v: ventral.

Fig. 6 Nasal region of *Huso dauricus* surface model (corresponding to the right nasal region of specimen). (A) Lateral aspect (box, Fig. 3A). α: angle at which lateral wall of incurrent nostril inclined to body axis. (B) Anterior aspect (left box, Fig. 3B). (C) Dorsal aspect (box, Fig. 3C). Arrow 1 indicates lateral wall of incurrent nostril faces anteriorally, arrow 2 that excurrent nostril faces laterally. CS: Central support; EN: excurrent nostril; IN: incurrent nostril; *L*: characteristic dimension of nasal region; La: olfactory lamella; NB: nasal bridge; SC: sensory channel (extent indicated by dashed lines); W (and dashed line): incurrent nostril wall; XY: extent of sagittal cross-section used to calculate Reynolds number for flow through the nasal chamber (Section 2.7.3).

Fig. 7 Olfactory rosettes of *Huso dauricus* surface model. (A) Anterolateral aspect of right nasal region (right box, Fig. 3B). (B) Cut-away of (A) to show olfactory rosette. Sensory channels marking quadrant limits of olfactory rosette are numbered. Dashed line: position of incurrent nostril. Upper inset: two gaps (disks) between olfactory lamellae and central support. Gap on left connects sensory channels 10 and 11, gap on right sensory channels 7 and 8. Lower inset: cross-section through sensory channel marked by asterisk/small curved lines in main image. (C) Olfactory rosette of left nasal region. White frames in (B) and (C) indicate the lateral (Lt), dorsal (Do), medial (Me), and ventral (Ve) quadrants of rosette. Yellow and red disks:

channels through which dye passage observed or inferred, respectively. Black disks: bent olfactory lamellae. a: Anterior; CS: central support; d: dorsal; EN: excurrent nostril; Ey: eye; IN: incurrent nostril; *L*: characteristic dimension of sensory channel; La: olfactory lamella; p: posterior; SC: sensory channel; v: ventral; W: incurrent nostril wall.

Fig. 8 Schematics of olfactory flow in the plastic model of *Huso dauricus*. The plastic model is represented by the surface model. Panels (A) – (M) correspond to Video clips 1-13, respectively. The surface model orientation in each panel is based on a screenshot from the respective video clip. Insets in (C), (F) – (K) show which channels (numbered) dye passes through in the corresponding video clip. (N) Reference image. (A), (C) – (M): lateral views. (B) Dorsal view. Large white arrows in (A), (B) and (N): direction of free-stream flow. Other arrows indicate behaviour of dye. Scale bar in (N) also applies to (C) – (M). Lt, Do, Me and Ve: lateral, dorsal, medial and ventral quadrants of olfactory rosette, respectively. CS: Central support; EN: excurrent nostril; Ey: eye; IN: incurrent nostril; NR: nasal region; V1-3: vortices.

Fig. 9 Correspondence of CFD-generated streamlines to olfactory flow in the plastic model of *Huso dauricus*. Streamline(s) (tubes) correspond to dye behaviour in: (A) Video clip 4; (B) Video clip 12; and (C) Video clip 13. Large arrow in (A): direction of free-stream flow in (A) – (C). Do and Me: Streamlines arising from passage through (numbered) sensory channels in the dorsal and medial quadrants of olfactory rosette, respectively (cf. Fig. 7C). EN: Excurrent nostril; Ey: eye; IN: incurrent nostril; V1-3: vortices.

Fig. 10 Incurrent nostril entry points for CFD-generated streamlines passing through the olfactory sensory channels in the nasal chamber of the *Huso dauricus* model. Dashed line: contour enclosing region of fluid where speed of flow is ≥ 8 cm s^{-1}. White regions: areas through which (A) lateral (Lt), (B) dorsal (Do), (C) medial (Me), (D) ventral (Ve), and (E) all 'sensory channel' streamlines pass. Scale bar in (E): 0.25 mm. d: Dorsal; l: lateral; m: medial; v: ventral.

Fig. 11 Static pressure on the surface of *Huso dauricus* CFD model. Surface colour-coded according to pressure coefficient (*Cp*, panel B). (A) Anterior aspect of head. (B) Anterior and (C) lateral aspect of nasal region. Cross in (A) and (B), arrow in (C): direction of free-stream flow (into page for cross). Disks: points of relatively high static pressure. White line in (C): main division between $Cp > 0$ (red) and $Cp < 0$ (blue). Ba: Barbel; CB: position of cartilaginous

bar; EN: excurrent nostril; Ey; eye; IN: incurrent nostril; NR: nasal region; Ro: rostral tip; W: incurrent nostril wall.

Fig. 12 CFD-generated streamlines in the nasal chamber of the *Huso dauricus* model. Single streamlines (yellow tubes) passing through the sensory channels of the (A) lateral (Lt), (B) dorsal (Do), (C) medial (Me), and (D) ventral (Ve) quadrants of the right olfactory rosette. For clarity, not all of the streamlines passing through the dorsal and medial sensory channels are shown. Sensory channels marking the limits of streamline groups are numbered, and highlighted by disks, as are other sensory channels of note. Olfactory rosette colour-coded according to pressure coefficient (*Cp*, panel B). Dashed lines in (B) and (C): streamlines passing through (lateral) sensory channel 3 and (ventral) sensory channel 23, respectively. Scale bar in (D) also applies to (A) – (C). a: Anterior; CS: central support; EN and IN: position of excurrent and incurrent nostril, respectively; La: olfactory lamella; p: posterior; SC: sensory channel; V1, V2, and V4 (white streamline tube): vortices.

Fig. 13 CFD-generated streamlines showing flow decelerating as it approaches the central support of the olfactory rosette of the *Huso dauricus* model. Compare with Video clip 5 and Fig. 8E. Arrows, asterisk, and black on white lines: direction of flow, central support, and positions of incurrent (IN) and excurrent nostrils (EN), respectively. Streamlines colour-coded according to speed (*U*). La: Olfactory lamella; SC: sensory channel.

Fig. 14 Static pressure on the surface of *Pseudoscaphirhynchus kaufmanni* CFD model. Surface colour-coded according to pressure coefficient (*Cp*, panel C). (A) Anterior and (B) lateral aspect of head. Arrow: direction of free-stream flow. Yellow dot: location of probe used to monitor static pressure in transient CFD simulation. Inset in (B): magnified view of nasal region (slightly different orientation to main image). α: angle at which lateral wall of incurrent nostril inclined to body axis. White line: main division between $Cp > 0$ (red) and $Cp < 0$ (blue). (C) Anterior aspect of nasal region. Inset: anterolateral view of nasal region. Disks: points of relatively high static pressure. Cross: free-stream flow into page. White asterisks: eye; yellow asterisk: olfactory rosette's central support. CB: Position of cartilaginous bar; *Cp*: pressure coefficient; EN: excurrent nostril; IN: incurrent nostril; NR: nasal region; Ro: rostral tip; Sp: spines (Vecsei and Peterson, 2004); W: incurrent nostril wall.

Fig. 15 Nasal regions of *Acipenser schrenckii* (BMNH 1925.8.6.3) and *Scaphirhynchus platorynchus* (BMNH 1852.8.16.26) specimens. (A) Lateral, (B) anterolateral, and (C) anterior

954 view of right nasal region of *A. schrenckii*. (D) Anterior view of right nasal region of *S.*
955 *platorynchus*. All images flipped horizontally. CS: Central support; EN: excurrent nostril; Ey:
956 eye; IN: incurrent nostril; NF: nasal flap; Sp: spine; W: incurrent nostril wall.
957
958 **Fig. 16** CFD-generated streamlines in the (translucent) left nasal region of the
959 *Pseudoscaphirhynchus kaufmanni* model. Dorsal aspect. Compare with Video clip 15. Arrow:
960 direction of free-stream flow. Upper inset: enlargement (rotated and horizontally flipped – see
961 triangular marker) of bracketed area in main image. Lower inset: dorsal view of left head. Box:
962 location of main image. Scale bar: 2 cm. EN: Excurrent nostril; Ey: eye; IN: incurrent nostril;
963 NC: nasal chamber; V (and asterisk): vortex.
964

Video

Dye visualisation with the plastic sturgeon models. Flow is left to right and the free-stream speed is 5 cm s^{-1}. Unless stated otherwise: the model is that of *Huso dauricus*; pitch, yaw, and roll are 0°; the model is in orientation I, being viewed from flume face X (Fig. 4B); and each clip is flipped horizontally.

Clip 1 Passage of dye over head and through nasal chamber. Left lateral (slightly posterior) aspect. Compare with Fig. 8A.

Clip 2 Passage of dye over head and through nasal chamber. Right nasal region, dorsal aspect. Orientation II, flume face Y (Fig. 4B). Compare with Fig. 8B.

Clip 3 Passage of dye through olfactory sensory channels 1 and 24 to 26 (24 – 25 s). Left nasal region, lateral (slightly posterior) aspect. Compare with Fig. 8C.

Clip 4 Passage of dye through nasal chamber. Left nasal region, lateral aspect. Compare with Fig. 8D.

Clip 5 Fanning of dye in vicinity of central support of olfactory rosette. Right nasal region, lateral aspect. Orientation II (Fig. 4B). Clip rotated by 180°. Compare with Fig. 8E.

Clip 6 Passage of dye through sensory channels 1 to 3 (45 – 46 s) and 23 and 24 (43 – 44 s). Right nasal region, anterolateral aspect. Orientation II (Fig. 4B). Clip rotated 180°. Compare with Fig. 8F.

Clip 7 Passage of dye through sensory channels 1 and 22 to 24 (54 – 56 s). Right nasal region, anterolateral aspect. Pitch - 5°, flume face Z (Fig. 4B). Clip not flipped or rotated. Compare with Fig. 8G.

Clip 8 Passage of dye through sensory channels 20 to 23 (1 min 7 s to 1 min 8 s). Right nasal region, lateral aspect. Pitch - 5°, flume face Z (Fig. 4B). Clip not flipped or rotated. Compare with Fig. 8H.

Clip 9 Passage of dye through sensory channels 3 to 5 (1 min 13 s to 1 min 15 s). Left nasal region, lateral aspect. Compare with Fig. 8I.

Clip 10 Passage of dye through sensory channels 1 and 2 (1 min 18 s to 1 min 20 s), 17 and 18 (1 min 20 s onwards) and 24 to 26 (1 min 21 s). Left nasal region, anterolateral aspect. Pitch + 5°. Compare with Fig. 8J.

Clip 11 Passage of dye through sensory channels 4, 5 (1 min 30 s) and 6 (1 min 31 s to 1 min 32 s). Right nasal region, lateroventral aspect. Orientation III, roll + 34° (Fig. 4B). Clip rotated 180°. Compare with Fig. 8K.

Clip 12 Vortices in nasal chamber. Left nasal region, lateral aspect. Compare with Fig. 8L.

Clip 13 Vortex in nasal chamber. Left nasal region, lateral aspect. Compare with Fig. 8M.

Clip 14 Passage of dye through (translucent) nasal chamber of plastic model of *Pseudoscaphirhynchus kaufmanni*. Left nasal region, lateral aspect. Orientation III, roll + 90°, flume face Y (Fig. 4B). Clip not flipped or rotated.

Clip 15 Dye behaviour in (translucent) nasal chamber of plastic model of *Pseudoscaphirhynchus kaufmanni*. Left nasal region, dorsal aspect. Orientation III, roll - 90° (Fig. 4B). Clip rotated 180°. Compare with Fig. 16.

Clip 16 Separation of flow from back of head. Left laterodorsal aspect.

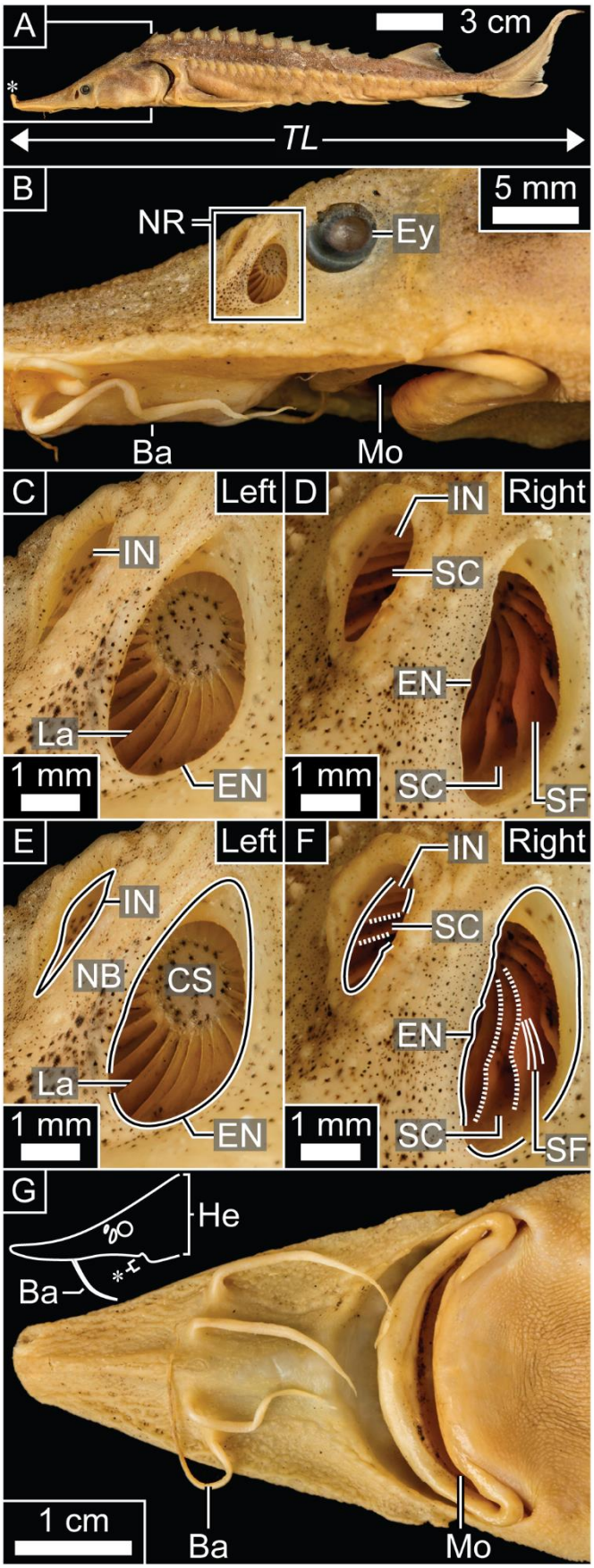

1007

1008

1009 **Fig. 1 Specimen of *Huso dauricus* (BMNH 1925.8.6.2) used to generate the models for**

1010 **fluid dynamics.**

1011

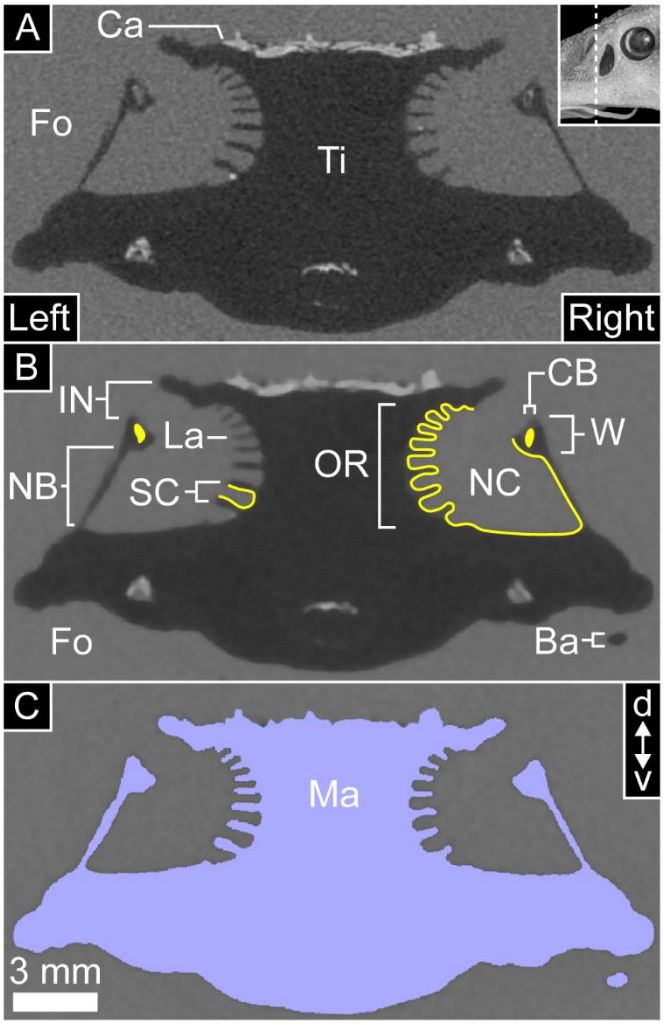

1012

1013

1014 **Fig. 2 Image processing.**

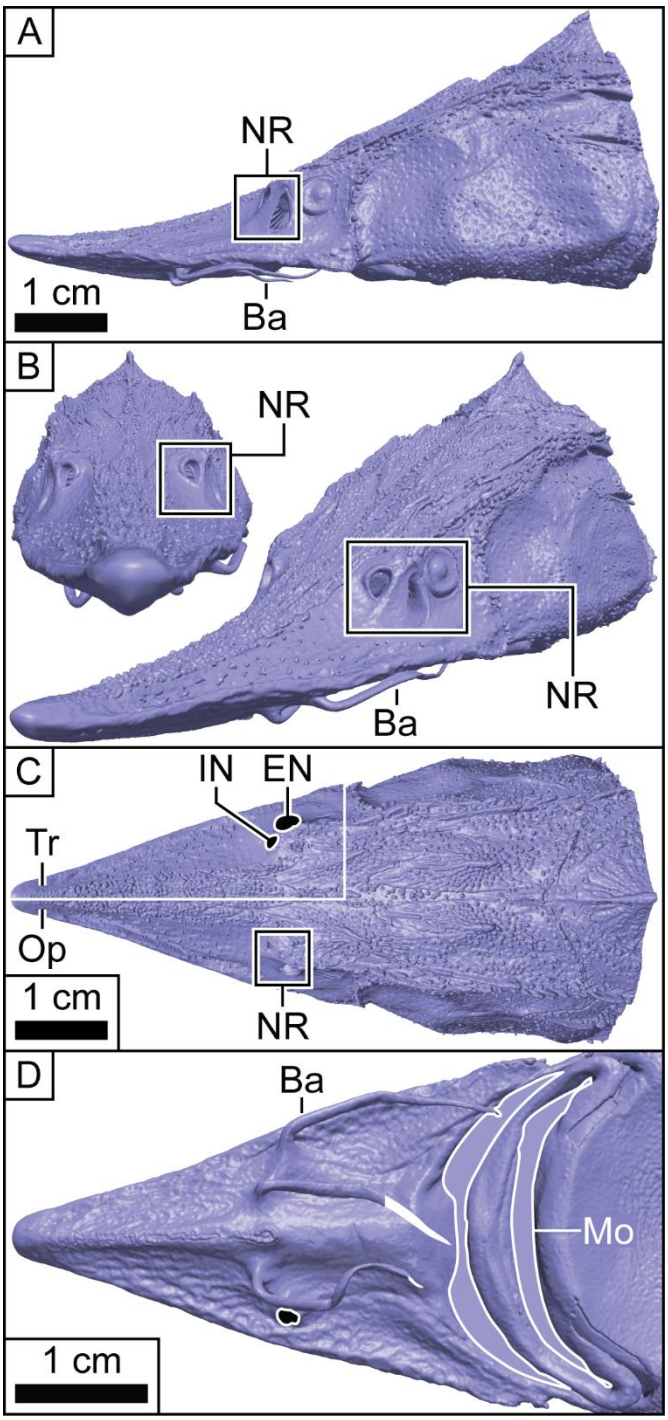

1015

1016

1017 **Fig. 3 Surface model of *Huso dauricus*.**

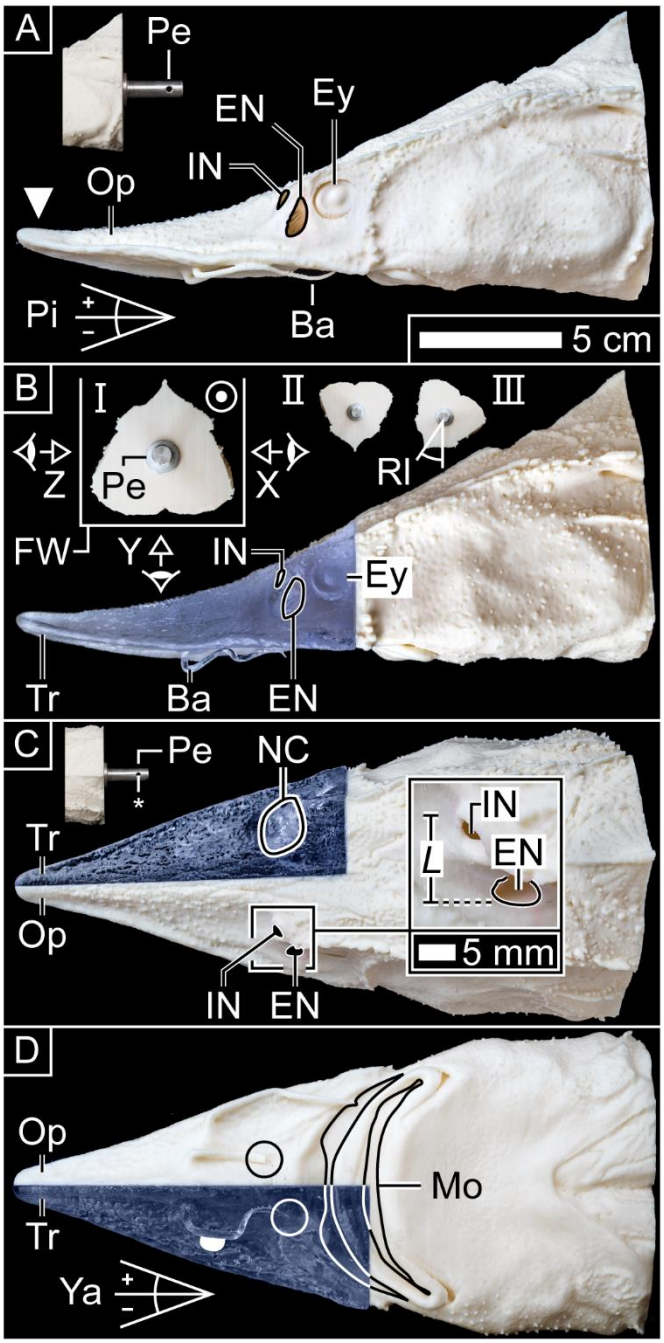

1018

1019

1020 **Fig. 4 Plastic model of *Huso dauricus*.**

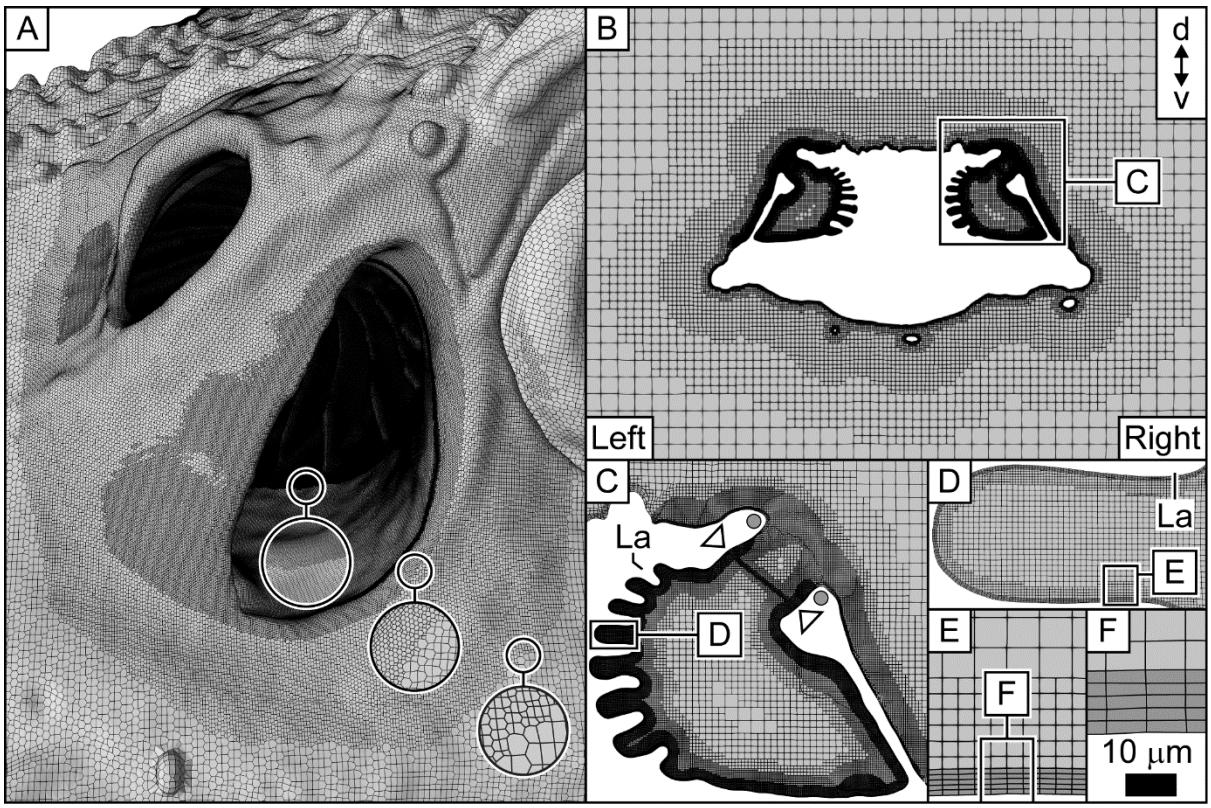

1021

1022

1023 **Fig. 5 CFD mesh of *Huso dauricus*.**

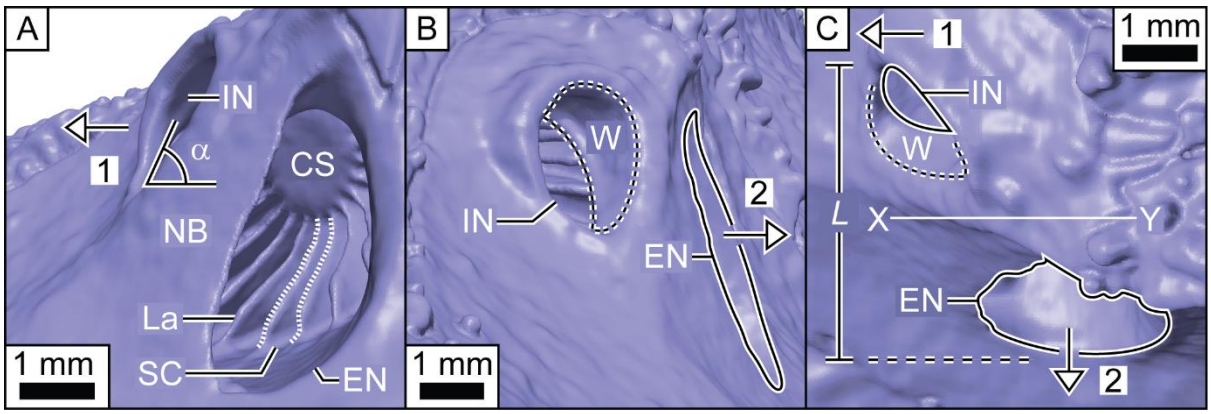

Fig. 6 Nasal region of *Huso dauricus* surface model (corresponding to the right nasal region of specimen).

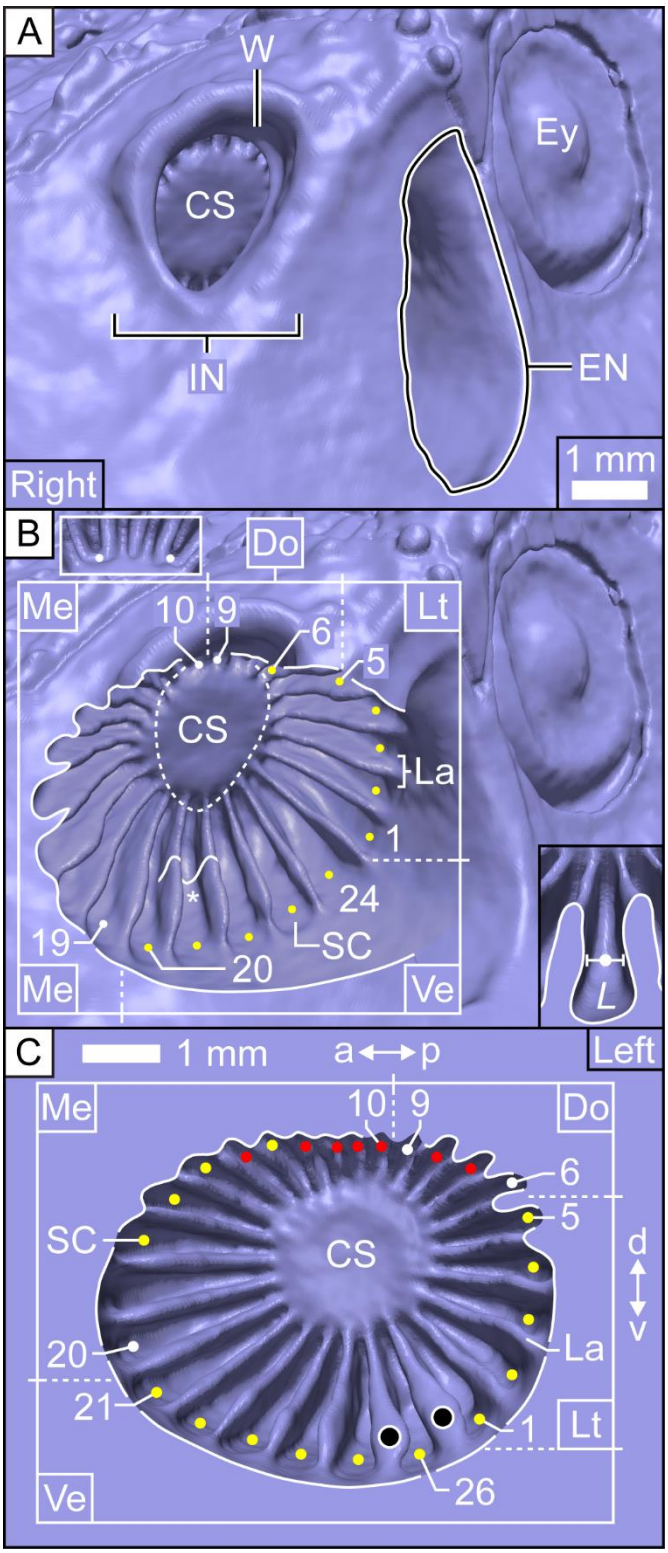

1028

1029

1030 **Fig. 7 Olfactory rosettes of *Huso dauricus* surface model.**

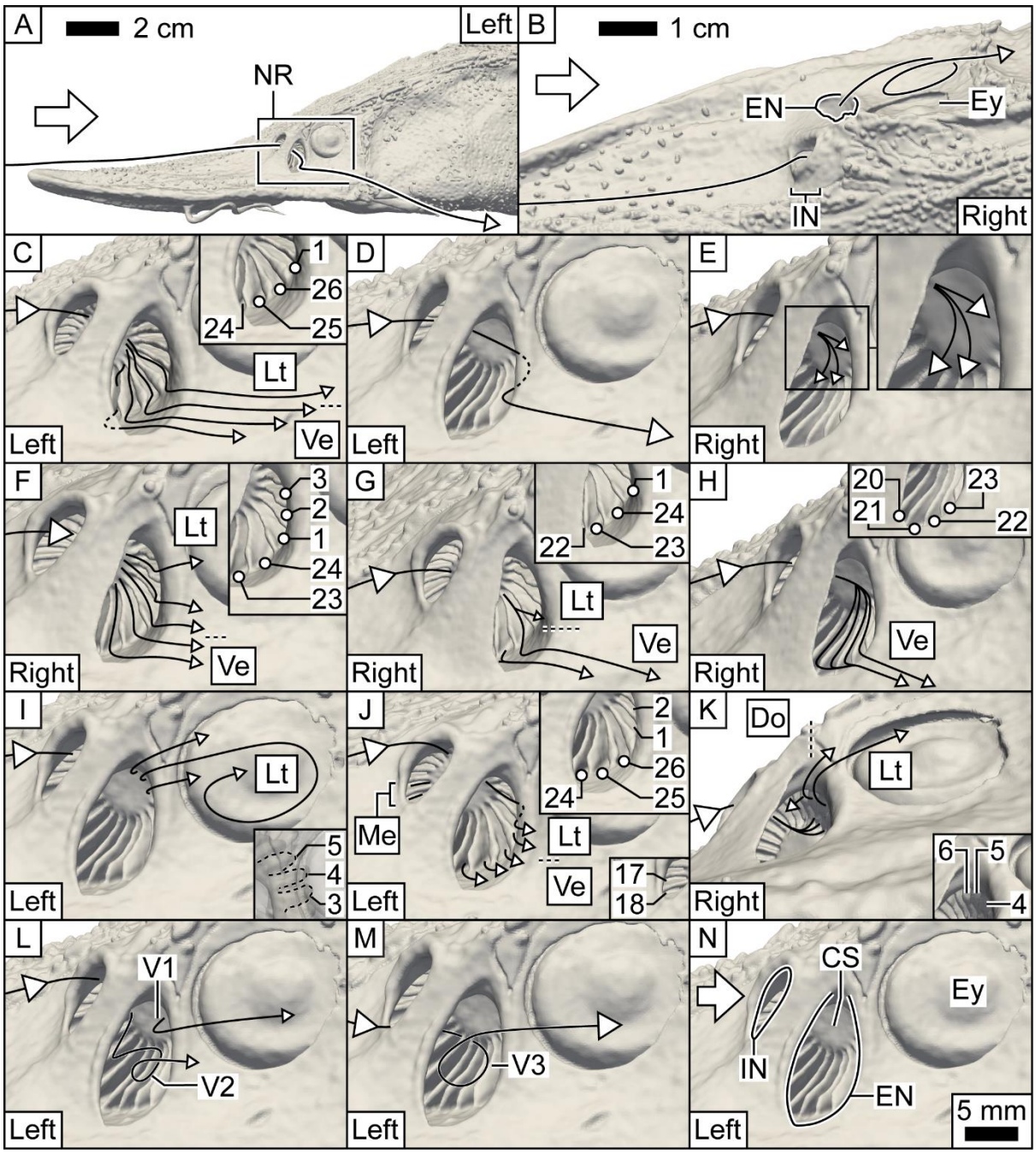

Fig. 8 Schematics of olfactory flow in the plastic model of *Huso dauricus*.

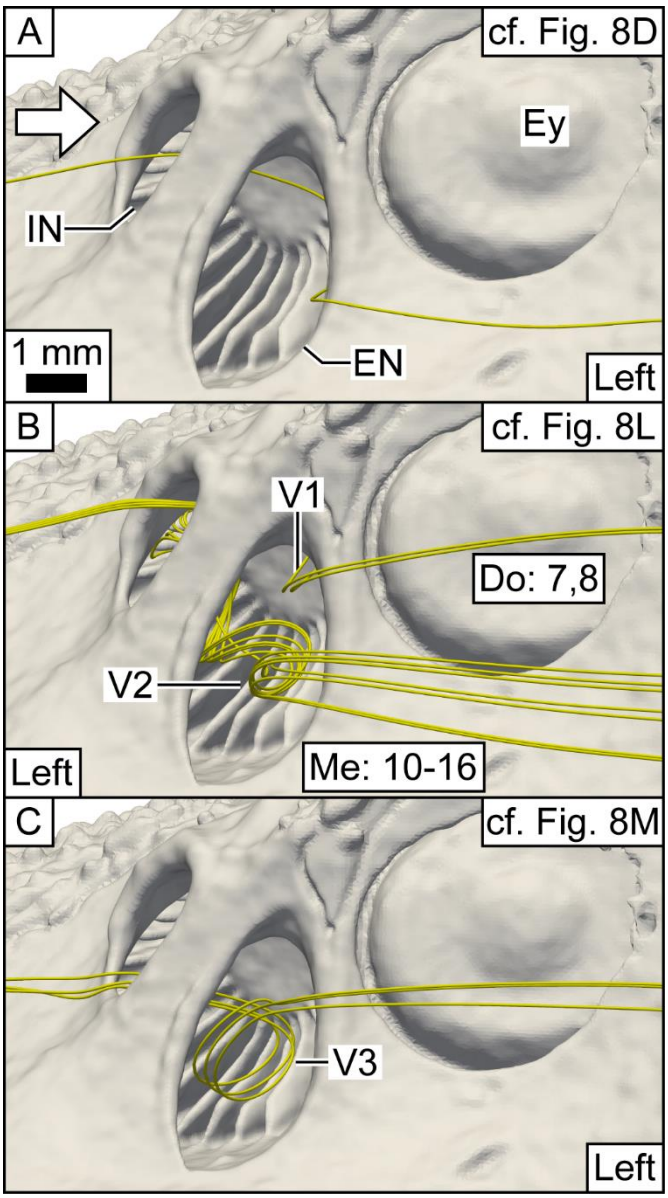

Fig. 9 Correspondence of CFD-generated streamlines to olfactory flow in the plastic model of *Huso dauricus*.

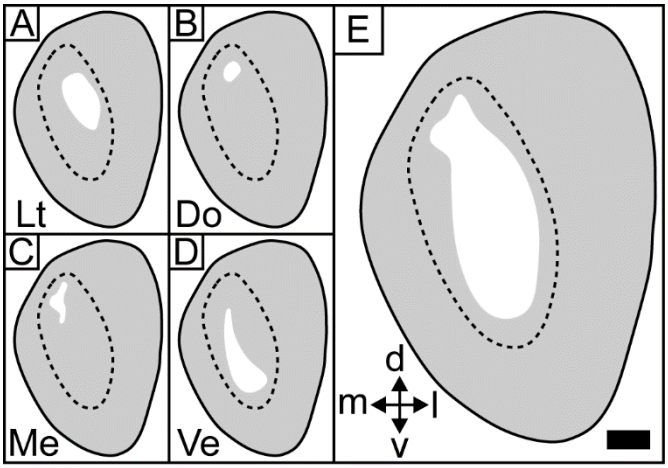

Fig. 10 Incurrent nostril entry points for CFD-generated streamlines passing through the olfactory sensory channels in the nasal chamber of the *Huso dauricus* model.

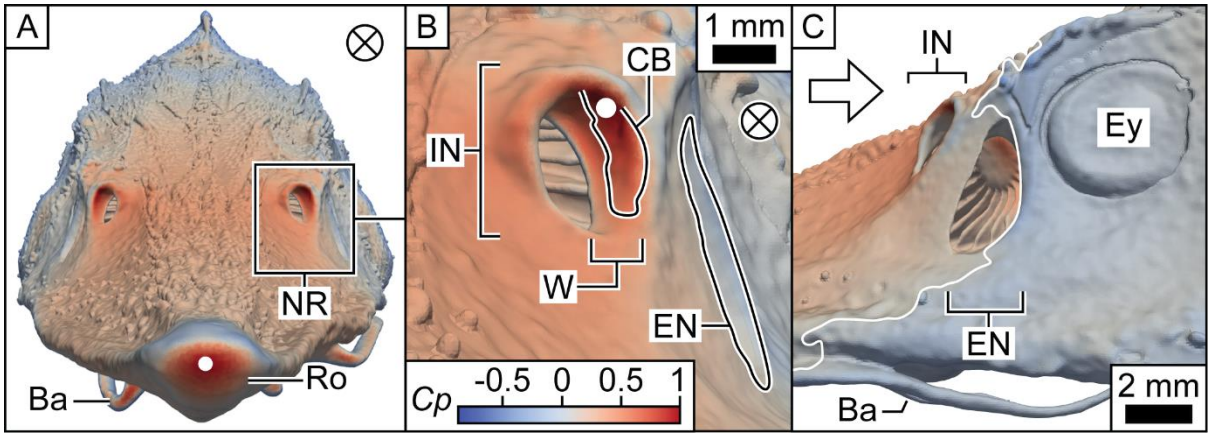

Fig. 11 Static pressure on the surface of *Huso dauricus* CFD model.

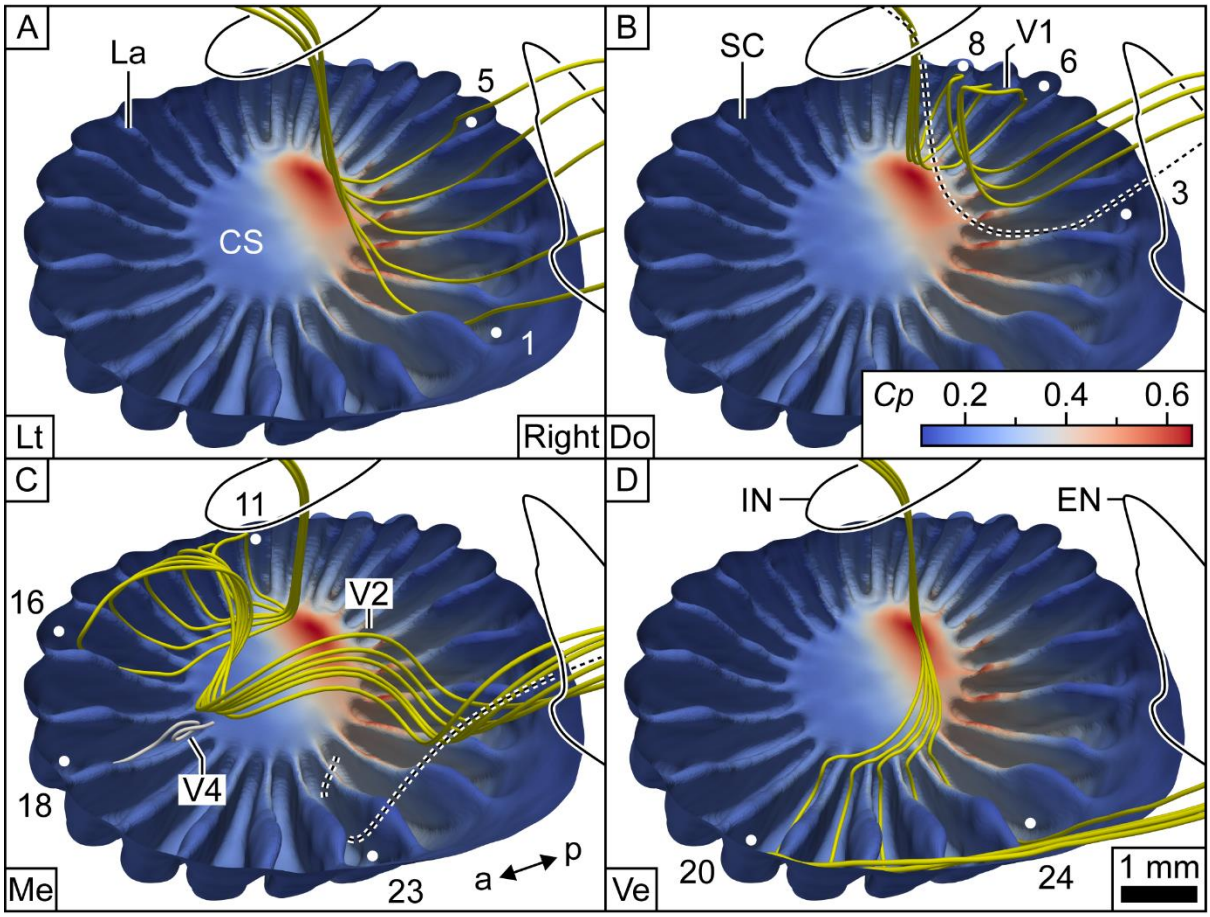

Fig. 12 CFD-generated streamlines in the nasal chamber of *Huso dauricus* model.

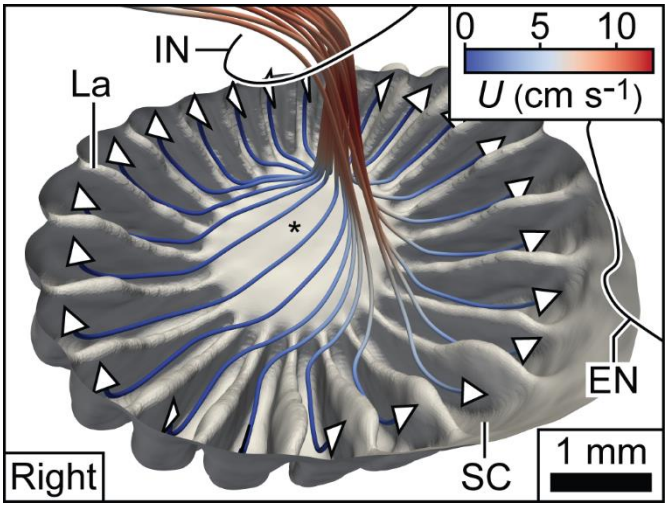

Fig. 13 CFD-generated streamlines showing flow decelerating as it approaches the central support of the olfactory rosette of the *Huso dauricus* model.

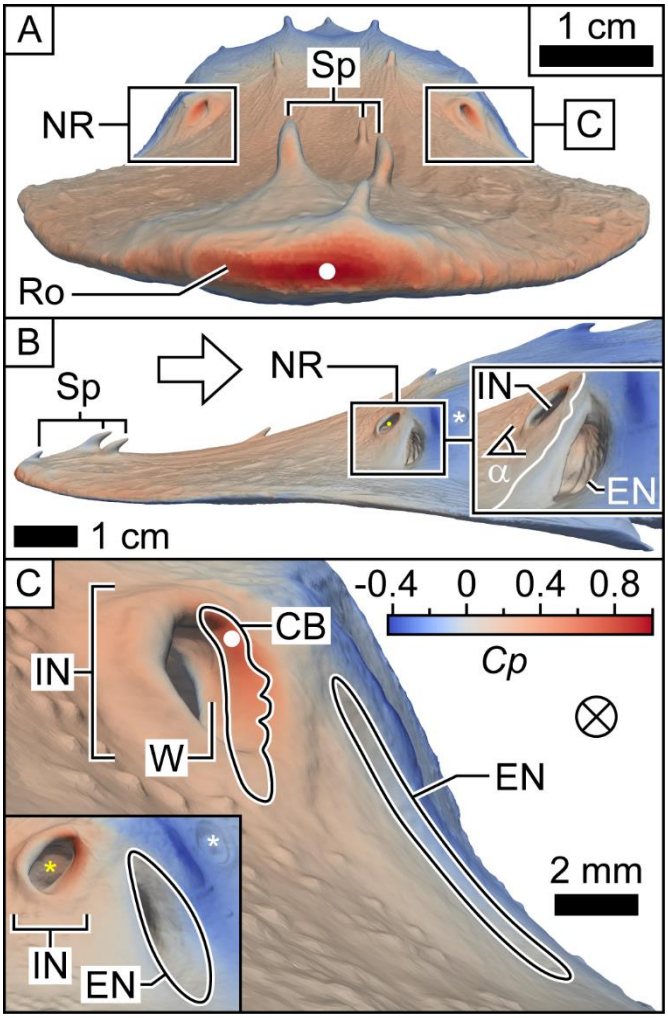

Fig. 14 Static pressure on the surface of *Pseudoscaphirhynchus kaufmanni* CFD model.

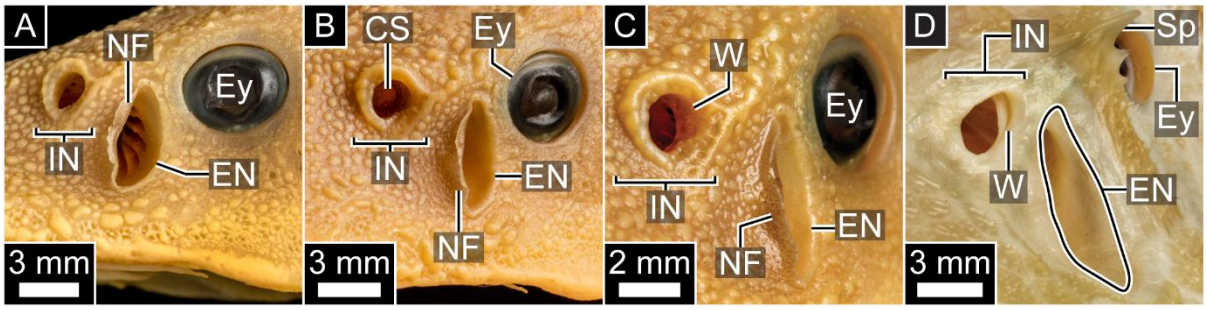

Fig. 15 Nasal regions of *Acipenser schrenckii* (BMNH 1925.8.6.3) and *Scaphirhynchus platorynchus* (BMNH 1852.8.16.26) specimens.

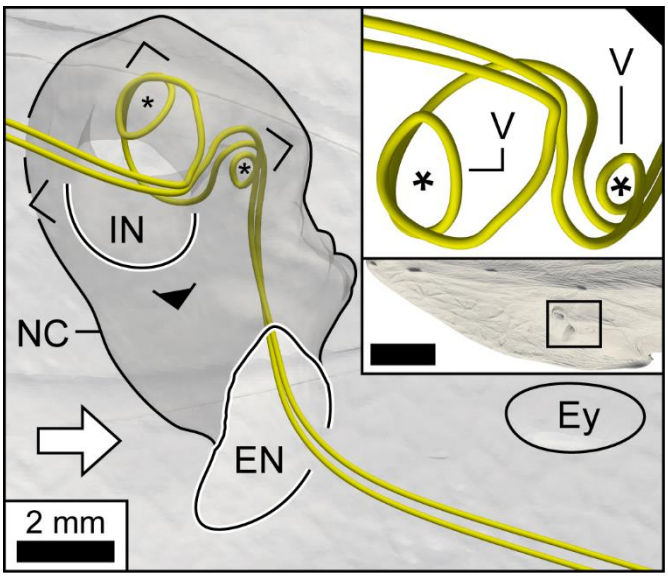

Fig. 16 CFD-generated streamlines in the (translucent) left nasal region of the *Pseudoscaphirhynchus kaufmanni* model.

Olfactory Flow in the Sturgeon is Externally Driven

Russell J. Garwood[a], Julia Behnsen[b], Harriet Haysom[c], Jeremy N. Hunt[d], Luke J. Dalby[e], Samuel K. Quilter[e], James S. Maclaine[f], Jonathan P. L. Cox[c*]

[a]*School of Earth and Environmental Sciences, University of Manchester, Manchester, M13 9PL, UK*

[b]*Henry Moseley X-ray Imaging Facility, University of Manchester, Manchester, M13 9PY, UK*

[c]*Department of Chemistry, University of Bath, Bath, BA2 7AY, UK*

[d]*Jeremy Hunt Design, Unit A6, 66 Norlington Road, London, E10 6LA, UK*

[e]*TotalSim, Top Station Road, Brackley, NN13 7UG, UK*

[f]*Department of Life Sciences, Natural History Museum, Cromwell Road, London, SW7 5BD, UK*

*Corresponding author
Dr Jonathan P.L. Cox
Department of Chemistry
University of Bath
Bath, BA2 7AY, UK
Tel. +44 1225 386548
j.p.l.cox@bath.ac.uk

Appendix A

A.1. Additional methodology

A.1.1. X-ray micro-computed tomography

The specimen of *Huso dauricus* was held in a plastic cylinder during the micro-CT scan, with the body axis of the specimen vertical and the head up. To prevent the specimen moving, a strip of muslin was wrapped around the body. The X-ray beam was generated from a static tungsten reflection target and passed through a 0.25 mm copper filter. Exposure time (single image), accelerating voltage, and current were 708 ms, 145 kV, and 85 μA, respectively. A total of 3142 projections were collected in a single 360° rotation at 0.114577° intervals. The projections were transformed into a 3D matrix using CT Pro 3D 2.2 (Nikon Metrology). Prior to converting the scan to a set of 8-bit TIFFs, the contrast between pixels corresponding to the tissue of the specimen and those corresponding to Fomblin was improved (using Drishti) by making a non-linear adjustment to the histogram of greyscale values.

A.1.2. Surface models

TIFF images from the micro-CT scan of *H. dauricus* were segmented with ScanIP's Threshold tool. To avoid capturing pixels corresponding to Fomblin, which had greyscale values lying between those of the pixels corresponding to the tissue and those corresponding to the cartilaginous skeleton (Fig. 2A), 'tissue' and 'cartilage' pixels were captured separately by the thresholding process, creating 'tissue' and 'cartilage' masks. The tissue and cartilage masks were then joined with the Boolean operations tool (Union with) to create a mask of the complete head ('head' mask). To facilitate the joining process, prior to the Boolean Union operation a Morphological filter (Dilate) was applied to the cartilage mask, using a Structuring element (ball) with a radius of one pixel in the x, y, and z directions. The Floodfill, Paint, and 3D editing (Cuboid) tools were used to remove the barbel, to seal the mouth, to put a hole in the back of the 'opaque' mask (below) for the plastic model's aluminium peg (Fig. 4A-C, Pe), and to fill internal cavities (to reduce the size of the STL file prior to 3D printing/conversion to the CFD mesh). For the reason explained in Appendix A.1.3, the head mask was reflected through its median plane (Evans, 1993, p. xi) with the Flip tool. The size of the head mask was adjusted with the Rescale tool. To make the plastic model, two new masks were created, one ('opaque' mask) corresponding to the plastic model's opaque part (Fig. 4A), the other ('translucent' mask) to the translucent part (Fig. 4B).

The translucent mask was isolated from the head mask with the Floodfill tool. The opaque mask was generated with the Boolean operations tool by subtracting the translucent mask from the head mask. A surface model was created from each mask with the following features (de)selected in ScanIP's 'Model configuration' dialogue box: a) 'General' tab → Smart mask smoothing (pre-processing) → Use greyscale values; b) 'Surface settings' tab → Triangle smoothing → Use triangle smoothing for masks (10 iterations); and c) 'Surface settings' tab → Decimation → Decimate box unticked.

A.1.3. Plastic model

We considered the left nasal region of the *H. dauricus* specimen to be more suitable for dye visualisation than the right, because the anterior edge of the left excurrent nostril appeared more robust and smoother than its right counterpart (cf. Fig. 1C and D). Consequently the left nasal region was chosen to become the translucent part of the plastic model. This meant, however, that the model would be upside down when observed from the flume's most convenient viewing face (Fig. 4B, face X). Consequently, to return the model to its upright state, the surface model was, during its preparation, reflected through its median plane (Appendix A.1.2). Thus the plastic model's (opaque) left nasal region (Fig. 4A) corresponds to the specimen's right nasal region, and the plastic model's (translucent) right nasal region (Fig. 4B) corresponds to the specimen's left nasal region. Similarly, the CFD model's left nasal region corresponds to the specimen's right nasal region, and the CFD model's right nasal region corresponds to the specimen's left nasal region.

A.1.4. Fluid dynamics

A.1.4.1. Dye visualisation

The plastic model of *H. dauricus* was suspended in the flume using the rig described in Abel et al. (2010). The model was fixed to the rig via its aluminium peg (Fig. 4A-C, Pe). One of the holes in the peg (Fig. 4C, asterisk) allowed the model to be upright or upside down (orientations I and II, Fig. 4B). The rig/peg arrangement also allowed the pitch, yaw, and roll (Barnard and Philpott, 2004) of the model to be varied (Fig. 4A, B and D). The model was positioned such that it was central (± 2 cm) width-wise to the working section of the flume. The maximum transverse cross-sectional area of the model was 61 cm^2, less than 5% of the working cross-sectional area of the flume. Therefore, based on standard corrections (Barlow et al., 1999, p. 361), the effect of the walls of the flume on flow in the vicinity of the model is likely to have been negligible. The model was illuminated with a halogen lamp or an LED

light panel. A white sheet was placed behind the model to help visualise dye. The dye solution was introduced from a reservoir under constant pressure using stainless steel tubing (internal diameter 1.3 mm, external diameter 2.0 mm). The horizontal section of this tubing, from which dye was released, was 25 cm from the flume's floor. At a free-stream speed of 5 cm s^{-1}, dye emerged from the tubing as a well-defined filament, indicating that the exit velocity of the dye was equal to the local flow velocity (Fig. 3.1 of Lim, 2000); at free-stream speeds > 5 cm s^{-1}, however, the dye filament became turbulent. To minimise the effect of the tubing on flow over the model, the aperture of the tubing was located some distance (10 – 11 cm) upstream from the point of impingement on the model (Lim, 2000). We observed dye behaviour in the nasal chamber mainly through the excurrent nostril (e.g. Fig. 8C), but also through the incurrent nostril (Fig. 8J) and through the translucent plastic corresponding to the specimen's left nasal region (Fig. 8I).

A.1.4.2. Computational fluid dynamics

The tail (Fig. A.2) was added to the back of the *H. dauricus* STL model with GeoMagic Wrap, essentially as follows. The posterior surface of the model was replicated (Polygons → Boundaries → Create → Boundary By Crease Angle [18°]) and offset caudally (Polygons → Offset → Offset Entire Model [23.2 cm]). The posterior edge of the model was extruded (Polygons → Boundaries → Move → Extrude Boundary [2 cm]), and then joined to the offset posterior surface with a series of ~ 50 bridging surfaces (Polygons → Fill Holes → Fill Single → Bridge → Flat), and the gaps between the bridging surfaces filled (e.g. Polygons → Fill Holes → Fill Single → Bridge → Curvature). Prior to joining, the offset posterior surface was reduced in size (Tools → Transform → Scale). The scaled offset surface, together with the offset distance, gave the tail a taper angle of 7° (Fig. A.2), which from previous CFD simulations was known to prevent flow separating from the back of a model. The tail was smoothed (e.g. Polygons → Smooth → Relax) and imperfections in the model removed (Polygons → Mesh Doctor, e.g. with Self-Intersections and Small Tunnels boxes ticked).

Points of relatively high static pressure on the surface of the *H. dauricus* CFD model were located using ParaView's Find Data tool.

The average static pressure in the excurrent nostril was calculated in ParaView by first using the Slice filter to put through the mesh a plane that passed through the excurrent nostril, and then applying to that plane the following succession of filters: Connectivity → Threshold (to

isolate the segment of the plane within the excurrent nostril) → Calculator (to calculate the static pressures at all points within this segment) → Integrate Variables. The average pressure was then found by dividing the 'pressure' entry (Attribute: Point Data) in the Spreadsheet view by the Area entry (Attribute: Cell Data).

Streamlines were generated by applying the Stream Tracer With Custom Source filter to either a point or line, with the following menu selections (selections in brackets): Vectors (velocity); Interpolator Type (Interpolator with Point Locator); Integration Direction (Both); Integrator Type (Runge-Kutta 4.5); Integration Step Unit (Cell Length); Initial Step Length (0.2 m); Minimum Step Length (0.01 m); Maximum Step Length (0.5 m); Maximum Steps (2000); Maximum Streamline Length (0.2 m); Terminal Speed (10^{-12} m s^{-1}); Maximum Error (10^{-6}). The point or line was created from the Sources menu (Point Source or Line).

To designate the white areas shown in the insets of Fig. 10, a line of five equally spaced points was first placed along the length of each sensory channel. A streamline was generated from each point. The white areas were then designated with the Clip filter, using a plane that passed through the nostril and the relevant group of streamlines.

A.1.5. Nasal chamber volumes

The volume of each nasal chamber of the *H. dauricus* model was calculated using ScanIP, as follows. The Floodfill tool was used to create from the head mask a mask corresponding to the Fomblin. The 3D editing (Cuboid) tool was then used to cut the Fomlin mask flush to both the incurrent and excurrent nostril apertures, and the nasal chamber volume isolated with the Floodfill tool. This volume was then converted to a surface model as described in Appendix A.1.2. The volume of the nasal chamber surface model was read from the Model Statistics tab.

A.1.6. Reynolds numbers for olfactory flow through nasal chamber (CFD simulation)

The volumetric flow rate through each nasal chamber of *H. dauricus* was determined in ParaView by first using the Slice filter to put through the mesh a plane that passed through the nasal chamber (Fig. 6C, line XY) and then applying the following succession of filters: Connectivity → Threshold (to isolate the segment of the plane within the nasal chamber) → Surface Vectors (to select velocity vectors perpendicular to the nasal chamber segment) → Calculator (to determine the magnitude of the velocity vectors) → Integrate Variables. The wetted perimeter of the nasal chamber was estimated from a perpendicular view of the

segment by importing the view into Rhinoceros, tracing the outline of the segment with the Free-Form command (Curve → Free-Form → Control Points), and then calculating the length of the line with the Length command (Analyze → Length).

A.2. Effect of reflecting Huso dauricus *model*

Given the symmetrical fluid environment for both the dye visualisation experiments and the CFD simulation (Section 2.5), we assumed that reflecting the model of *H. dauricus* (Appendix A.1.2) would not affect olfactory flow. We tested this assumption by observing dye behaviour in the opaque nasal region (Fig. 4A) when the model was both upright and upside down in the flume (orientations I and II, Fig. 4B). Dye behaved similarly in both cases (cf. Video clip 5, orientation II, with Video clip 8, orientation I). Furthermore, flow behaved similarly in both nasal regions despite their mild asymmetry (Section 3.1). Therefore reflecting the model had little or no effect on olfactory flow.

A.3. Additional references

Barlow, J.B., Rae, W.H., Pope, A., 1999. Low-Speed Wind Tunnel Testing. 3rd ed. John Wiley & Sons, New York.

Barnard, R.H., Philpott, D.R., 2004. Aircraft Flight. 3rd ed. Pearson Education, Harlow.

Evans, H.E., 1993. Miller's Anatomy of the Dog. 3rd ed. W.B. Saunders Company, Philadelphia.

A.4. Heads of other sturgeon species inspected in this study

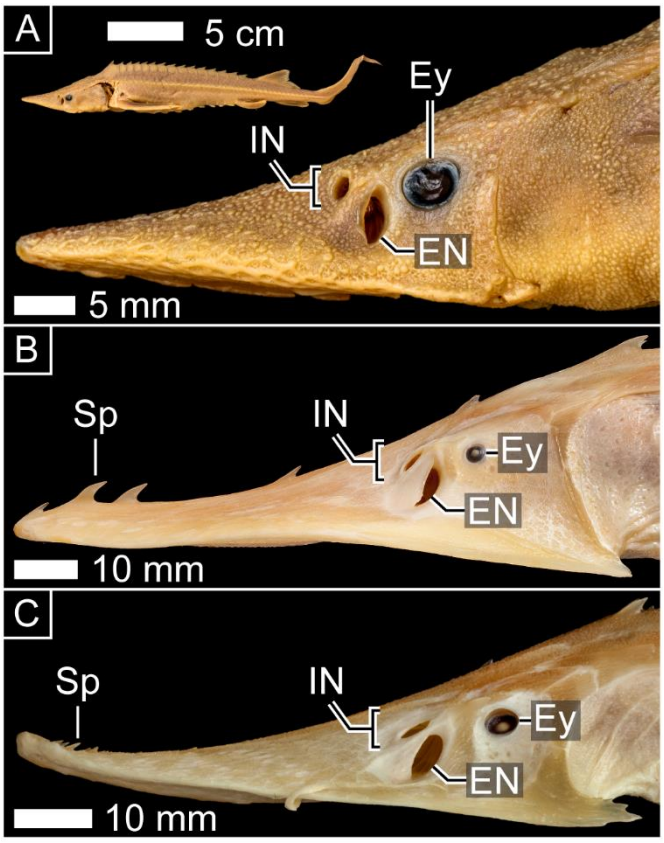

Fig. A.1. Heads of other sturgeon species inspected in this study. (A) *Acipenser schrenckii* (BMNH 1925.8.6.3). Entire specimen shown above main image. (B) *Pseudoscaphirhynchus kaufmanni* (BMNH 1887.4.5.17). Image flipped horizontally. (C) *Scaphirhynchus platorynchus* (BMNH 1852.8.16.26). Image flipped horizontally. EN: Excurrent nostril; Ey: eye; IN: incurrent nostril; Sp: spine.

A.5. CFD model of Huso dauricus

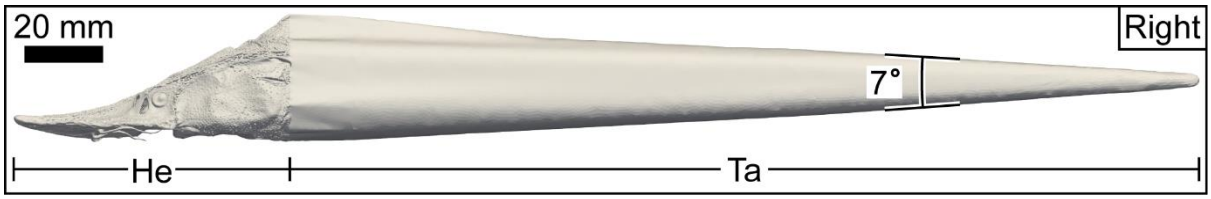

Fig. A.2. CFD model of *Huso dauricus*. He: Head; Ta: tapered extension (‘tail’).

A.6. Variation in static pressure in transient CFD simulation of Pseudoscaphirhynchus kaufmanni *model*

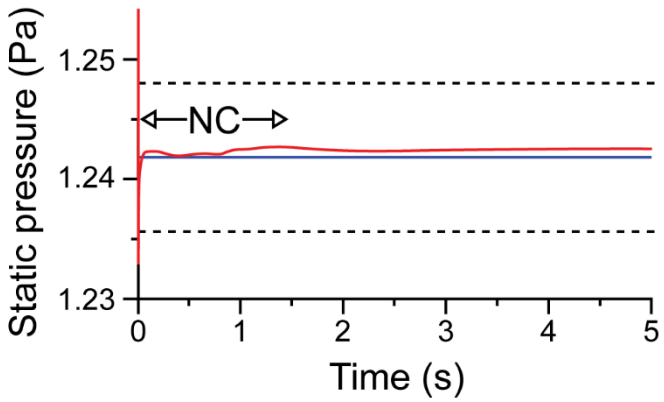

Fig. A.3. Variation in static pressure in transient CFD simulation of *Pseudoscaphirhynchus kaufmanni* model. Static pressure monitored in centre of left incurrent nostril (Fig. 14B, yellow dot). Red line: variation in static pressure. Blue line: average static pressure in last 500 iterations of steady-state simulation (Section 2.5.2). Dotted lines indicate 0.5% deviation from this average. NC: time taken for nasal chamber to be flushed once in steady-state simulation. Maximum subsequent deviation between red and blue lines = 0.07%. Simulation conditions identical to those for *Huso dauricus* model (Section 2.5.2).